

1 **Accurate Elucidation of Oxidation Under Heavy Ozone**
2 **Pollution: A Full Suite of Radical Measurement In the**
3 **Chemical-complex Atmosphere**

4 Renzhi Hu¹, Guoxian Zhang^{1,2,✉}, Haotian Cai¹, Jingyi Guo¹, Keding Lu⁴, Xin Li⁴,
5 Shengrong Lou⁵, Zhaofeng Tan⁴, Changjin Hu¹, Pinhua Xie^{1,3,✉✉}, Wenqing Liu^{1,3}

6 ¹ Key Laboratory of Environment Optics and Technology, Anhui Institute of Optics and Fine
7 Mechanics, HFIPS, Chinese Academy of Sciences, Hefei, China

8 ² School of Physics and New Energy, Xuzhou University of Technology, Xuzhou, China

9 ³ College of Resources and Environment, University of Chinese Academy of Science, Beijing, China

10 ⁴ State Key Joint Laboratory of Environmental Simulation and Pollution Control, College of
11 Environmental Sciences and Engineering, Peking University, Beijing, China

12 ⁵ State Environmental Protection Key Laboratory of the Formation and Prevention of Urban Air
13 Pollution Complex, Shanghai Academy of Environmental Sciences, Shanghai, China

15 **✉Correspondence to:** Guoxian Zhang, School of Physics and New Energy, Xuzhou
16 University of Technology, Xuzhou, China

17 **✉✉Correspondence to:** Pinhua Xie, Key Laboratory of Environment Optics and
18 Technology, Anhui Institute of Optics and Fine Mechanics, HFIPS, Chinese Academy of
19 Sciences, Hefei, China

20 **Email addresses:** gxzhang@aiofm.ac.cn (Guoxian Zhang); phxie@aiofm.ac.cn (Pinhua
21 Xie)

22

23 **Abstract:** The Yangze River Delta (YRD) in China encountered with prolonged ozone
24 pollution in September 2020. To accurately elucidate the limitations of oxidation
25 processes in the chemical-complex atmosphere, a full suite of radical measurements (OH,
26 HO₂, RO₂, and k_{OH}) was established in YRD region for the first time. The diurnal peaks
27 of radicals exhibited considerable variation due to environmental factors, showing ranges
28 of 3.6 to $27.1 \times 10^6 \text{ cm}^{-3}$ for OH, 2.1 to $33.2 \times 10^8 \text{ cm}^{-3}$ for HO₂, and 4.9 to $30.5 \times 10^8 \text{ cm}^{-3}$
29 for RO₂. The simulated results provided by the RACM2-LIM1 mechanism failed to
30 adequately match the observed data both in radical concentration and experimental
31 budget at a heavy ozone pollution episode. Sensitivity tests utilizing a comprehensive set
32 of radical measurements revealed that the higher aldehyde mechanism (HAM) effectively
33 complements the regeneration of OH radicals, yielding enhancements of 4.4% - 6.0%
34 compared to the base scenario, while the concentrations of HO₂ and RO₂ radicals have
35 shown increments of about 7.4% and 12.5%, respectively. It is noteworthy that under the
36 constraints of k_{OH} measurement, the inclusion of OVOCs and larger alkoxy radicals
37 derived from monoterpenes improved the model-measurement consistency for ozone
38 formation, reducing the discrepancy under high NO conditions from 4.17 to 2.39. This
39 outcome corroborates the hypothesis of sensitivity analysis as it pertains to ozone
40 formation. Moving forward, by implementing a comprehensive radical detection
41 approach, further investigations should concentrate on a broader range of OVOCs to
42 rectify the imbalance associated with RO₂ radicals, thereby providing a more precise
43 understanding of oxidation processes during severe ozone pollution episodes.

44

45 **Keywords:** FAGE-LIF; Full-chain detection; Radical; P(Ox); OVOCs;

46

47 1 Introduction

48 In recent years, China's rapid economic development has led to severe environmental
49 pollution problems, which significantly impacted the respiratory, dermatological, and visual
50 health of local residents (Wang et al., 2022c; Huang et al., 2018). This has raised
51 concerns about the coexistence of regional primary and secondary pollution, making air
52 quality improvement efforts a focal point (Liu et al., 2021; Wang et al., 2022a). In the
53 complex atmosphere, near-surface ozone (O_3) is formed through continuous
54 photochemical reactions between nitrogen oxides ($NO_x \equiv NO + NO_2$) and volatile
55 organic compounds (VOCs) under light conditions, while hydroxyl radicals (OH) serve
56 as the main oxidant in the troposphere, converting VOCs into hydroperoxy (HO_2) and
57 organic peroxy (RO_2) radicals (Rohrer et al., 2014; Hofzumahaus et al., 2009).
58 Additionally, the oxidation of nitric oxide (NO) and peroxy radicals produce nitrogen
59 dioxide (NO_2), which is the sole photochemical source of ozone (Lu et al., 2012; Stone et
60 al., 2012).

61 Despite numerous experimental and theoretical explorations to establish the
62 radical-cored photooxidation mechanism in the troposphere, field observations were
63 primarily focused on HO_x ($HO_x \equiv OH + HO_2$) radicals due to the limitations of detection
64 technology (Kanaya et al., 2012; Lu et al., 2012; Hofzumahaus et al., 2009; Yugo Kanaya
65 and Tanimoto, 2007; Ren et al., 2008; Stone et al., 2012; Levy, 1971). Recent
66 advancements in detection technology, such as the application of a new LIF technique
67 (RO_x LIF), have made the detection of RO_2 radicals possible (Whalley et al., 2013; Tan et
68 al., 2017a). Moreover, the union of comprehensive field campaigns and box model, has
69 proven to be an effective method for verifying the integrity of radical chemistry at local
70 to global scales (Lu et al., 2019b; Tan et al., 2018). Several experiments have indicated
71 that the existing atmospheric chemical mechanism posted challenges in deepening the
72 understanding of the regional pollution explosion (Whalley et al., 2021; Slater et al., 2020;
73 Tan et al., 2017a; Woodward-Massey et al., 2023). For instance, the observation of up to
74 $4 \times 10^9 \text{ cm}^{-3}$ of RO_2 radical in the center of Beijing in 2017 (APHH) was significantly
75 underestimated by the MCM v3.3.1 mechanism (Whalley et al., 2021). Further exploring
76 the unreplicable concentration and the oxidation process in the chemical-complex
77 atmosphere is deemed necessary (Whalley et al., 2021; Woodward-Massey et al., 2023).

78 The YRD region, situated between the North China Plain (NCP) and Pearl River
79 Delta (PRD), is highly prone to regional transport interactions and aerosol-boundary layer
80 feedback (Jia et al., 2021; Huang et al., 2020). In an effort to gain a better understanding
81 between the complex radical chemistry and the intensive oxidation level in the Yangze
82 River Delta, TROPSTECT-YRD (The experiment on Radical chemistry and Ozone
83 Pollution perSpectively: long-Term Elucidation of the photochemiCal oxidaTion in the
84 Yangze River Delta) was conducted in Hefei during September 2020. Accurate
85 elucidation of the oxidation process under heavy ozone pollution was provided by a full
86 suite of radical measurement (OH , HO_2 , RO_2 and k_{OH}) in the chemical-complex
87 atmosphere.

88 **2 Materials and methods**

89 **2.1 Site description and instrumentation**

90 The TROPSTECT observation was conducted from 1 to 20 September 2020 at the
91 Science Island background station (31.9° N, 117.2° E) in Hefei, a typical megacity located
92 in the central region of Anhui Province within the Yangtze River Delta. The station is
93 situated on a peninsula with abundant vegetation to the northwest of urban areas and is in
94 close proximity to Dongpu Lake, which is only 200 meters away, and the main road,
95 positioned 250 meters southward (Fig. 1). Consequently, the relatively enclosed
96 environment exhibits typical suburban characteristics of anthropogenic emissions. The
97 station is located in the transition region between urban and suburban areas, reflecting the
98 regional transpor of pollution in Hefei and its surrounding areas.



99
100 **Fig. 1.** (a) The location of the measurement site (source: © Google Earth).
101 (b) The close shot of the measurement site location (source: © Google Earth).
102 (c) The actual image for the LIF-Box.

103 Regarding the instrumentation, a group of oxidation-related instruments were
104 installed on the 7th floor of the Comprehensive Building at the Anhui Institute of Optics

105 and Fine Mechanics (AIOFM), with all sampling outlets positioned more than 20 meters
106 above the ground. The details of the instruments measuring various parameters such as
107 meteorological factors (WS, WD, T, RH, P, Jvalues), gas pollutants (O₃, CO, SO₂, NO,
108 NO₂, HONO, HCHO, PAN), and non-methane hydrocarbons (NMHCs) are provided in
109 Table S1.

110 The measurement of NO, NO₂, O₃, CO, and SO₂ was carried out using commercial
111 Thermo Electron model series instruments. Thereof, NO and NO₂ were measured using a
112 chemical fluorescence method (CL) with an enhanced trace-level NO-NO₂-NO_x analyzer
113 (PKU-PL), which achieved a detection limit of 50 ppt (Tan et al., 2017a). The detection
114 of O₃ and SO₂ was conducted through Thermo Electron model 49i and 43i, respectively,
115 while Thermo Electron model 48i was utilized for CO detection. Cavity ring-down
116 spectroscopy (CRDS, Picarro-G2401) was employed for CO detection in parallel, and
117 another ultraviolet absorption instrument (Ecotech EC9810B) was for ozone detection.
118 The instrument inlets were placed within 5 meters of each other for comparison.

119 To ensure measurement accuracy, the instruments in the campaign underwent zero
120 point calibration procedures during the early (August 31st) and late (September 21st)
121 observation periods, and cross-calibrations for O₃ and CO measurements were carried out
122 during the middle (September 9th). Furthermore, additional zero calibration for Thermo
123 48i CO detection was undertaken daily from 0:00-0:30 to minimize shift correction. The
124 comparison results revealed high consistency within the instrument accuracy range for
125 both CO and O₃ measurements (Fig. S1(a)(b)).

126 HONO was detected using a home-built instrument by cavity-enhanced absorption
127 spectroscopy (CEAS), while formaldehyde was determined by the Hantzsch method
128 (SDL MODEL 4050) (Duan et al., 2018; Yang et al., 2021a). An automated gas
129 chromatograph equipped with a mass spectrometer and flame ionization detector
130 (GC-FID/MS) was employed for the online measurement of 99 VOCs species.
131 Information table for parts of the VOC monitoring species by online GC-MS/FID was
132 listed in Table S2.

133 The eight crucial photolysis frequencies (j(NO₂), j(H₂O₂), j(HCHO_M), j(HCHO_R),
134 j(HONO), j(NO₃_M), j(NO₃_R), j(O¹D)) were directly measured by a photolysis
135 spectrometer (Metcon, Germany). The unmeasured photolysis frequencies of the

136 remaining active species were computed using Eq.(1):

$$j = l \cdot \cos(\chi)^m \cdot e^{-n \cdot \sec(\chi)} \quad (1)$$

137 The variations in photolysis frequency due to solar zenith angle (χ) were adjusted based
138 on the ratio of observed and simulated $j(\text{NO}_2)$. The optimal values for parameters (l , m ,
139 and n) for different photolysis frequencies were extensively detailed by the MCM v3.3.1
140 (http://mcm.york.ac.uk/parameters/photolysis_param.htm) (Jenkin et al., 2003; Jenkin et
141 al., 1997).

142 **2.2 Radical measurement**

143 **2.2.1 OH, HO₂, RO₂ Concentrations**

144 The laser-induced fluorescence instrument developed by the Anhui Institute of Optics
145 and Fine Mechanics (AIOFM-LIF) was used to simultaneously detect the concentrations
146 of OH, HO₂, and RO₂ radicals, along with OH reactivity (k_{OH}). The OH radical was
147 directly measured by detecting on-resonance fluorescence excited by a 308 nm laser. An
148 indirect measurement for HO₂ was carried out after converting it to OH at a fixed
149 efficiency (Heard and Pilling, 2003).

150 The laser utilized for fluorescence excitation is a high-frequency tunable dye laser
151 that emits a 308 nm laser, with the laser power divided into a ratio of 0.45:0.45:0.08:0.02.
152 Of this power, 90% is directed towards fluorescence cells for concentration and reactivity
153 detection via optical fibers, respectively. 8% of the laser power is directed to a reference
154 cell, while the remaining 2% is used to monitor real-time power fluctuations. The laser is
155 transmitted through HO₂, OH, and RO₂ cells in turn via a coaxial optical path. Two
156 photodiodes are set up at the end of the reference cell and RO₂ detection cell, respectively.
157 The voltage signals and power fluctuations are compared synchronously to diagnose the
158 laser stability. To maintain detection efficiency, the power inside the measurement cells
159 should not be less than 10 mW. Sampling nozzles of 0.4 mm are deployed above OH and
160 HO₂ cells for efficient sampling at a flow rate of approximately 1.1 SLM, and the
161 pressure for all fluorescence cells are maintained at 400 Pa. The micro-channel plate
162 (MCP) detects the weak fluorescence signal collected by lens systems with low noise and
163 high gain. Additionally, a digital delay generator (DG645) optimizes the timing control
164 between the laser output, signal detection, and data acquisition. All of these modules are
165 integrated into a sampling box with constant air conditioning, except for the laser.

166 The detection of RO₂ radicals is more complex compared to the integrated detection
167 of OH and HO₂ radicals (Whalley et al., 2013). To achieve the complete chemical
168 conversion from RO_x to HO₂, a crucial role is played by a 66 mm×830 mm aluminium
169 flow tube, whose performance has been confirmed through the CHOOSE-2019 field
170 campaign (Li et al., 2020). A mixture of 0.17% CO and 0.7 ppm NO injected into the
171 flow tube facilitates the reduction of heterogeneous radical loss and enhancement of
172 conversion efficiency. The sampling flow is limited to 7 SLM by a 1 mm nozzle, and the
173 tube pressure is maintained at 25 hPa. In contrast to the HO_x cells, the large-diameter
174 nozzle (4 mm) is equipped above the cell, and a high concentration of NO (~300 ppm)
175 facilitates the full magnitude HO₂→OH conversion.

176 The observation data (H₂O, O₃) is combined with experimental characterization to
177 eliminate ozone photolysis interference, and most interference signals are excluded by
178 utilizing wavelength modulation (Zhang et al., 2022a). A comparison experiment with
179 PKU-LIF demonstrated the consistency of OH measurement in complex atmosphere
180 (Zhang et al., 2022b). An additional atmospheric oxidation observation was conducted in
181 the same location and season in 2022 with a chemical modulation method to determine
182 the chemical background of OH radicals (Fig. S2). During the ozone pollution
183 (2022.9.29-2022.10.3), the daytime peaks of ozone concentration above 75 ppb,
184 accompanied by alkene species approaching ~10 ppb. The diurnal concentration of
185 isoprene was also a high level (>1 ppb). The chemical conditions are more favourable to
186 induce OH interference than in the TROPSTECT campaign, while the OH concentrations
187 achieved by chemical modulation (OH_{chem}) and wavelength modulation (OH_{wav}) were in
188 good agreement. No obvious chemical background was observed by deploying an inlet
189 pre-injector. While it was not anticipated that OH measurements would be influenced by
190 internal interference, the possibility of unknown interferences cannot be excluded since
191 titration tests were not employed during the campaign. Consequently, the OH
192 measurements represent an upper bound to the actual values.

193 For HO₂ measurement, lower NO concentration (~1.6 × 10¹² cm⁻³, corresponding to
194 ~15% conversion efficiency) are selected to limit the RO₂→HO₂ interference to less than
195 5% (Wang et al., 2021). Since only the total-RO₂ mode is used for the campaign, the
196 additional uncertainty introduced by RO₂/R(OH)O₂ classification is negligible (Tan et al.,

197 2017b). The observed maximum daily PAN (11:00-14:00) is only 1.15 ± 0.67 ppb,
198 resulting in a calculated PAN-pyrolytic interference for RO_2 measurement of less than 1
199 ppt (Fuchs et al., 2008). The general applicability of AIOFM-LIF in complex atmosphere
200 has been demonstrated through various campaigns (Zhang et al., 2022b; Wang et al.,
201 2021; Wang et al., 2019a).

202 To complete the calibration task, a standard source stably generates equal amounts
203 of OH and HO_2 radicals (Wang et al., 2020). The radical source is also capable of
204 yielding specific RO_2 by titrating hydrocarbon with OH. It is noteworthy that CH_3O_2 has
205 the highest mixing ratio in the RO_2 species, thus it was chosen to represent for sensitivity
206 calibration. The instrument is calibrated every two days, except during rainy weather. The
207 limit of detection (LOD) for OH, HO_2 , and RO_2 in different cells with a typical laser
208 power of 10 mW is measured at $3.3 \times 10^5 \text{ cm}^{-3}$, $1.1 \times 10^6 \text{ cm}^{-3}$, and $2.5 \times 10^6 \text{ cm}^{-3}$,
209 respectively (60 s, 1σ). Measurement accuracy for OH, HO_2 , and RO_2 radicals are
210 reported to be 13%, 17%, and 21%, respectively.

211 **2.2.2 OH reactivity(k_{OH})**

212 The detection of k_{OH} in the atmosphere, defined as the reciprocal of OH lifetime, was
213 conducted using a laser flash photolysis laser-induced fluorescence (LP-LIF) instrument
214 (Lou et al., 2010). The configuration structure for k_{OH} measurement has been detailed in a
215 previous study (Liu et al., 2019). The flow tube in the OH production-reaction unit is at
216 ambient pressure, with a gas flow rate of 17 SLM. A pulsed laser beam (266 nm with an
217 average power of 15 mJ) is output from a frequency-quadrupled Nd:YAG laser, which
218 generates stable OH radical through flash photolysis of ambient ozone in the flow tube.
219 Consistent and stable production of OH radicals is ensured by maintaining a stable
220 concentration of reactants, flow field, and laser energy. Under conditions of 80 ppb O_3
221 and 8000 ppm water vapor concentration, OH radicals produced in the flow tube remains
222 at the concentration order of 10^9 cm^{-3} . Subsequently, the OH radicals are sampled through
223 a nozzle into a fluorescence cell. The OH fluorescence signal is then detected using laser
224 pump and probe techniques and is fitted to calculate the slope of OH decay (k_{OH}). The
225 detection accuracy, achieved with an integration time of 180 s, is 0.3 s^{-1} (1σ).

226 **2.3 Observation-Based Model**

227 The Regional Atmospheric Chemical Mechanism version 2 (RACM2) incorporating

228 the latest Leuven isoprene mechanism (LIM) was utilized to simulate the concentrations
 229 and reactions of OH, HO₂, and RO₂ radicals (Stockwell et al., 1997; Griffith et al., 2013;
 230 Peeters et al., 2014). The RACM2-LIM1 mechanism was specifically involved with
 231 fewer species compared to the explicit MCM mechanism, thus ensuring higher
 232 operational efficiency (Liu et al., 2022). The comprehensive list of model constraints was
 233 provided in Table S3. The measured NMHCs include 29 alkanes, 11 alkenes, 15
 234 aromatics, as well as acetylene and isoprene. For the base scenario, boundary conditions
 235 were established using the observed species, with assumed concentrations of hydrogen
 236 (H₂) and methane (CH₄) at 550 ppb and 1900 ppb, respectively. An ozone-simulation test
 237 was conducted to determine the suitable atmospheric lifetime (τ_D) for the base model. At
 238 the lifetime of 24 hours, with a corresponding first-order loss rate of 1.1 cm/s (assuming a
 239 boundary layer height of 1 km), the simulated ozone concentration closely matched the
 240 observed values (Fig. S3). To improve the model-measurement consistency between OH,
 241 HO₂ and RO₂ radicals, a series of sensitivity analyses were performed to evaluate the
 242 impacts of potential mechanisms, as detailed in Table 1. The time resolution of all
 243 constraints was uniformly set to 15 minutes through averaging or linear interpolation. To
 244 reinitialize unconstrained species to a steady-state, three days of data were input in
 245 advance as the spin-up time.

246 **Table 1.** The sensitive test scenarios utilized to improve the model-measurement consistency between
 247 OH, HO₂ and RO₂ radicals.

Scenario	Configuration	Purpose
Base	RACM2 updated with isoprene reaction scheme (LIM)	The base case with the species involved in Table S3 are constrained as boundary conditions.
HAM on (4 × ALD)	As the base scenario, but add the reactive aldehyde chemistry, and the concentration of ALD was amplified by a factor of 4.	To quantify the impact of missing aldehyde primary emissions on ROx chemistry.
HAM on (4 × ALD+MTS)	As the HAM on (4 × ALD) scenario, but add a monoterpene source, and the monoterpene level is ~0.4 ppb.	Utilizing monoterpene-derived RO ₂ to represent the alkoxy radicals with rather complex chemical structures.
Ozone simulation	As the base scenario, but remove the constraints of the observed ozone and NO concentrations.	To test the suitable lifetime for the base model.
HCHO simulation	As the base scenario, but remove the constraint of the observed HCHO concentration.	To test the simulation effect of the existing mechanism on formaldehyde concentration.

248
 249 The local formation of ozone can be accurately quantified through the online
 250 measurement of ROx radicals (Tan et al., 2018). To overcome the interference from NO,

251 the total oxidant (Ox), which is defined as the sum of NO_2 and O_3 , can serve as a reliable
 252 parameter to indicate the level of oxidation. Eq.(2) shows that the rate of NO oxidation
 253 by peroxy radicals is equivalent to the production of O_3 , denoted as $F(\text{Ox})$:

$$254 \quad F(\text{O}_x) = k_{\text{HO}_2+\text{NO}}[\text{NO}][\text{HO}_2] + \sum_i k_{\text{RO}_2^i+\text{NO}}[\text{NO}]\text{RO}_2^i \quad (2)$$

255 The major loss pathways for Ox encompass ozone photolysis, ozonolysis reactions,
 256 and radical-related reactions ($\text{OH}/\text{HO}_2+\text{O}_3$, $\text{OH}+\text{NO}_2$), represented as $D(\text{Ox})$ in Eq.(3):

$$257 \quad D(\text{O}_x) = \varphi_{\text{OH}}j(\text{O}^1\text{D})[\text{O}_3] + \sum_i \{\varphi_{\text{OH}}^i k_{\text{Alkenes}+\text{O}_3}^i [\text{Alkenes}][\text{O}_3]\} + (k_{\text{O}_3+\text{OH}}[\text{OH}] + \\ 258 \quad k_{\text{O}_3+\text{HO}_2}[\text{HO}_2])[\text{O}_3] + k_{\text{OH}+\text{NO}_2}[\text{OH}][\text{NO}_2] \quad (3)$$

259 Here, the OH yields from ozone photolysis and ozonolysis reactions are denoted as φ_{OH}
 260 and φ_{OH}^i , respectively.

261 The net photochemical Ox production rate in the troposphere, denoted as $P(\text{Ox})$ in
 262 Eq.(4), can therefore be calculated as the difference between Eqs. (2) and (3):

$$263 \quad P(\text{O}_x) = F(\text{O}_x) - D(\text{O}_x) \quad (4)$$

264 2.4 Experimental budget analysis

265 In this study, an experimental radical budget analysis was also conducted (Eqs. (5)
 266 - (12)). Unlike model studies, this method relies solely on field measurements
 267 (concentrations and photolysis rates) and chemical kinetic data, without depending on
 268 concentrations calculated by models(Whalley et al., 2021; Tan et al., 2019b). Given the
 269 short-lived characteristics of OH, HO_2 , and RO_2 radicals, it is expected that the
 270 concentrations are in a steady state, with total production and loss rates being
 271 balanced(Lu et al., 2019a). By comparing the known sources and sinks for radicals,
 272 unknown processes for initiation, transformation and termination can be determined.

$$P(\text{OH}) = j_{\text{HONO}}[\text{HONO}] + \varphi_{\text{OH}}j(\text{O}^1\text{D})[\text{O}_3] + \sum_i \{\varphi_{\text{OH}}^i k_{\text{Alkenes}+\text{O}_3}^i [\text{Alkenes}][\text{O}_3]\} + (k_{\text{HO}_2+\text{NO}}[\text{NO}] + k_{\text{HO}_2+\text{O}_3}[\text{O}_3])[\text{HO}_2] \quad (5)$$

$$D(\text{OH}) = [\text{OH}] \times k_{\text{OH}} \quad (6)$$

$$P(\text{HO}_2) = 2 \times j_{\text{HCHO}_R}[\text{HCHO}] + \sum_i \{\varphi_{\text{HO}_2}^i k_{\text{Alkenes}+\text{O}_3}^i [\text{Alkenes}][\text{O}_3]\} + (k_{\text{HCHO}+\text{OH}}[\text{HCHO}] + k_{\text{CO}+\text{OH}}[\text{CO}])[\text{OH}] + \alpha k_{\text{RO}_2+\text{NO}}[\text{NO}][\text{RO}_2] \quad (7)$$

$$D(\text{HO}_2) = (k_{\text{HO}_2+\text{NO}}[\text{NO}] + k_{\text{HO}_2+\text{O}_3}[\text{O}_3] + k_{\text{HO}_2+\text{RO}_2}[\text{RO}_2]) + 2 \times k_{\text{HO}_2+\text{HO}_2}[\text{HO}_2][\text{HO}_2] \quad (8)$$

$$P(RO_2) = \sum i \left\{ \varphi_{RO_2}^i k_{Alkenes+O_3}^i [Alkenes][O_3] \right\} + k_{OH}[VOCs][OH] \quad (9)$$

$$D(RO_2) = \{(\alpha + \beta)k_{RO_2+NO}[NO] + (2 \times k_{RO_2+RO_2}[RO_2] + k_{HO_2+RO_2}[HO_2])\}[RO_2] \quad (10)$$

$$P(RO_x) = \sum i \left\{ (\varphi_{OH}^i + \varphi_{HO_2}^i + \varphi_{RO_2}^i) k_{Alkenes+O_3}^i [Alkenes][O_3] \right\} + j_{HONO}[HONO] + \varphi_{OH} j(O^1D)[O_3] + 2 \times j_{HCHO_R}[HCHO] \quad (11)$$

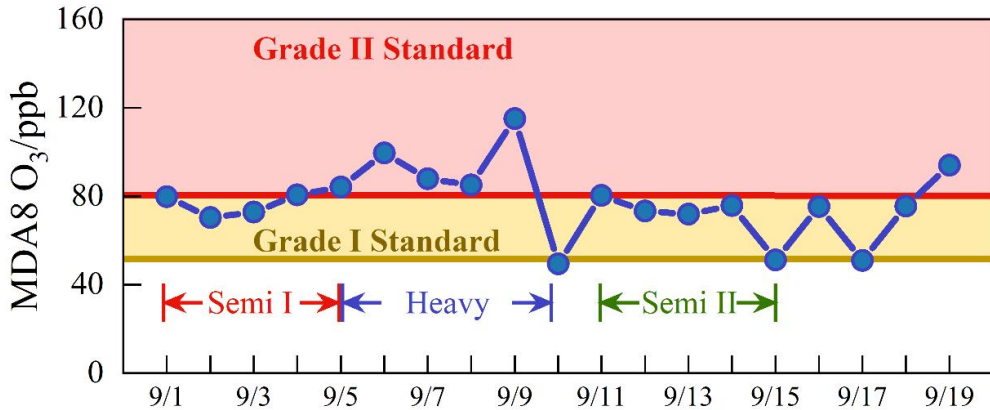
$$D(RO_x) = (k_{OH+NO_2}[NO_2] + k_{OH+NO}[NO])[OH] + \beta k_{RO_2+NO}[NO] + 2 \times (k_{RO_2+RO_2}[RO_2][RO_2] + k_{HO_2+RO_2}[HO_2][RO_2] + k_{HO_2+HO_2}[HO_2][HO_2]) \quad (12)$$

273 In which, $j(HONO)$, $j(O^1D)$ are the measured photolysis rates of HONO and O_3 ,
 274 respectively, and j_{HCHO_R} is the measured photolysis rate for the channel of
 275 formaldehyde photolysis generating HO_2 . φ_{OH} represent the OH yield in the O_3
 276 photolysis reaction. φ_{OH}^i , $\varphi_{HO_2}^i$ and $\varphi_{RO_2}^i$ are the yields for the ozonolysis reaction
 277 producing OH, HO_2 , and RO_2 , respectively. α is the proportion of RO_2 radicals reacting
 278 with NO that are converted to HO_2 , and β is the proportion of alkyl nitrates formation,
 279 which are set to 1 and 0.05, respectively(Tan et al., 2019b).

280 3 Results

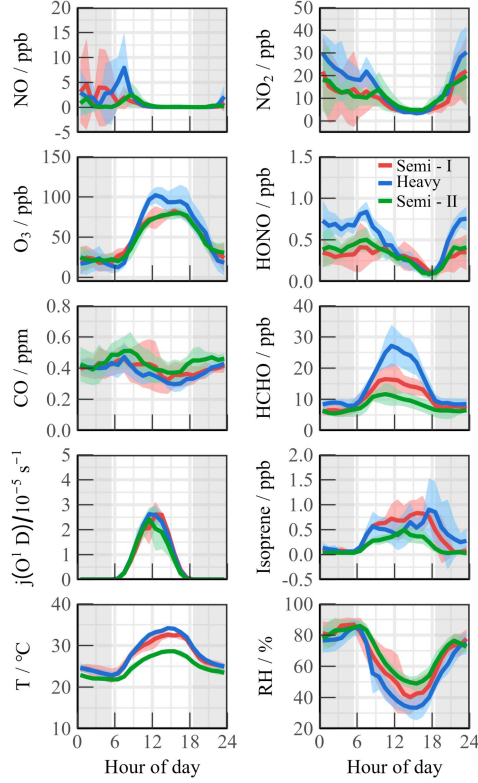
281 3.1 Overview of Measurement

282 During the observation period, the meteorological parameters and trace gas
 283 concentrations were plotted in Fig. S4. The timeseries revealed that the peak temperature
 284 exceeded 30°C, and the humidity levels remained between 30 – 50% during the daytime.
 285 The photolysis rates were observed to peak at noon (11:00 – 13:00), with $j(O^1D)$ and
 286 $j(NO_2)$ reaching approximately $3 \times 10^{-5} \text{ s}^{-1}$ and $8 \times 10^{-3} \text{ s}^{-1}$, respectively. Brief rainfall events
 287 temporarily happened on September 10th, 15th, and 17th, but totally favorable
 288 meteorologies induced the prolonged ozone pollution. The daily maximum 8-hour
 289 average ozone concentration (MDA8), as depicted in Fig. 2, consistently exceeded the
 290 Chinese Grade I national air quality standard (GB3095-2012) throughout the observation,
 291 with nine days exceeding the Grade II standard.



292
293 **Fig. 2.** The daily maximum 8 h average O_3 during the campaign. The yellow and red lines denote the Grade I and
294 Grade II national standards for O_3 , respectively. Brief rainfall events temporarily happened on 10, 15, and 17 Sep.
295

296 The ozone pollution can be categorized into three continuous periods based on
297 pollution levels, which disclose transitional ‘Semi - Heavy - Semi’ pollution
298 characteristics. Fig. 3 depicts daily variations in meteorological and trace gas
299 concentrations for different periods. During the Semi I (1 to 5 September) and Semi II (11
300 to 14 September) periods, the MDA8 levels exceeded Grade I standard, with an average
301 value of 75.92 ± 5.14 ppb and 75.45 ± 3.73 ppb, respectively. Notably, NO levels peaked
302 around 9:00 and rapidly decreased to a few hundred ppt due to photochemistry. In
303 addition, HONO and NO_2 exhibited bimodal variations, with diurnal concentration ranges
304 of 0.09 – 0.50 ppb and 3.35 – 13.77 ppb, respectively. The HONO/ NO_2 ratios during both
305 Semi periods were consistent with previous urban/suburban observations, with daytime
306 values of 0.049 ± 0.014 and 0.035 ± 0.012 , respectively (Yang et al., 2021b; Shi et al., 2020;
307 Hu et al., 2022). Isoprene levels accumulated during the day and decreased at night
308 during both Semi pollution episodes, with a diurnal average concentration in Semi II only
309 49.3% of that in Semi I (0.71 ± 0.087 ppb vs 0.35 ± 0.073 ppb). Formaldehyde, as the key
310 oxidation species, exhibited a concentration profile mirroring that of isoprene, with
311 significantly higher concentrations ranging from 1.20 to 36.34 ppb compared to other
312 urban regions (Ma et al., 2022; Yang et al., 2022; Tan et al., 2017b; Yang et al., 2021a).
313 Heavy pollution episodes from 5 to 9 September resulted in daytime ozone concentration
314 as high as 129.9 ppb, and oxidation-related species such as HCHO, HONO, NO_x , and
VOCs increased synchronously compared to other days.



315

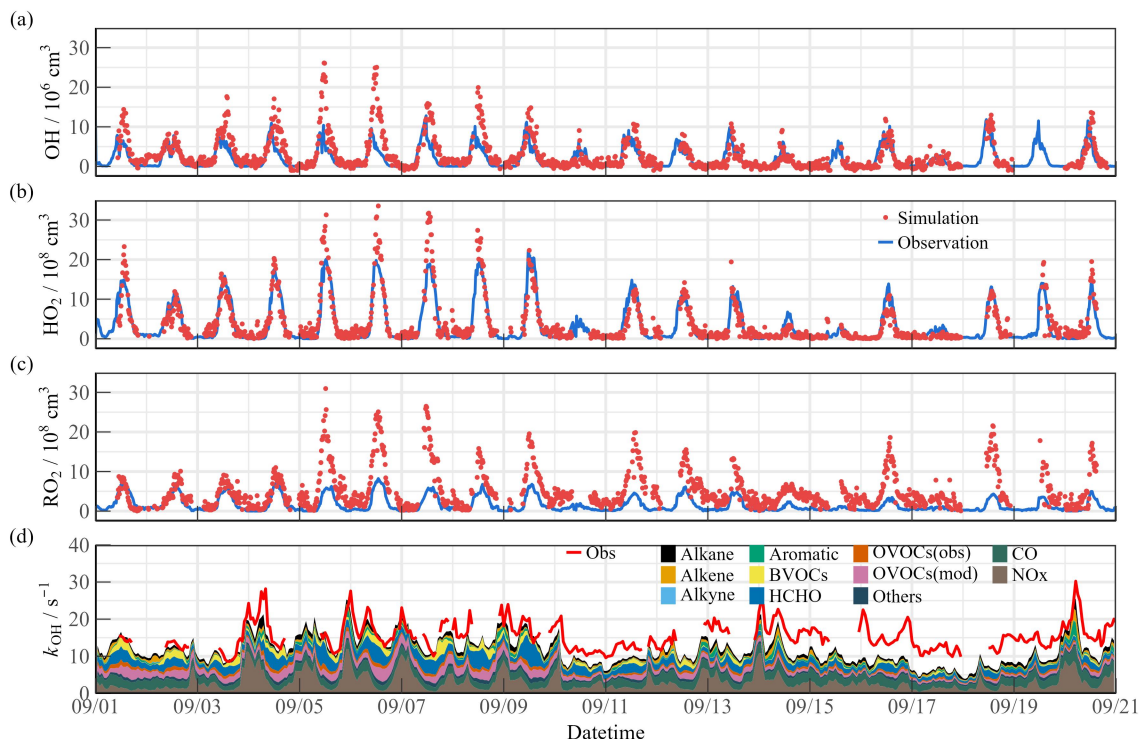
316
317

Fig. 3. Mean diurnal profiles of observed meteorological and chemical parameters during the campaign. Three periods were divided for subsequent study (Semi I, Heavy, and Semi II).

318 3.2 ROx radical concentrations and budgets

319 The observed and modeled timeseries for OH, HO₂, RO₂, and k_{OH} during the
 320 observation time are depicted in Fig. 4. The diurnal peaks of radicals exhibited a wide
 321 span due to changes in environmental conditions, with ranges of $3.6 - 27.1 \times 10^6 \text{ cm}^{-3}$ for
 322 OH, $2.1 - 33.2 \times 10^8 \text{ cm}^{-3}$ for HO₂, and $4.9 - 30.5 \times 10^8 \text{ cm}^{-3}$ for RO₂. Continuous data for
 323 k_{OH} observation were acquired within a range of $8.6 - 30.2 \text{ s}^{-1}$. Fig. S5 presents the
 324 diurnal profiles of the observed and modeled values during different episodes. The
 325 diurnal maximum of OH radical at noon differed between Semi I and Semi II, with
 326 $9.28 \times 10^6 \text{ cm}^{-3}$ and $5.08 \times 10^6 \text{ cm}^{-3}$, respectively, while total peroxy radicals (HO₂+RO₂)
 327 remained at similar levels with $19.43 \times 10^8 \text{ cm}^{-3}$ and $18.38 \times 10^8 \text{ cm}^{-3}$. Additionally, the
 328 distribution of peroxy radicals are not similar in the two Semi periods, with HO₂/RO₂
 329 ratios of 1.69:1 and 0.76:1, respectively, which reflects the uneven oxidation levels
 330 between Semi I and Semi II. During the Heavy ozone pollution, the averaged OH, HO₂,
 331 and RO₂ concentrations were 1.90, 2.15, and 1.98 times higher than those in the Semi
 332 periods, suggesting a stronger oxidation capacity, with k_{OH} in Heavy being 26.43% and

9.56% higher than in Semi I and Semi II, respectively. Limited anthropogenic emissions in the suburban environment reduced the oxidation contribution by NO_x and CO (27.59%). During the heavy pollution, organic species exhibited dominant behavior regarding diurnal reactivity (9.22 s⁻¹ for 69.79%), and anthropogenic hydrocarbons were not major k_{OH} sources. With an abundant level (~1 ppb), isoprene contributed more than 10% of the reactivity in the diurnal cycle. Therefore, the effect of BVOCs species (such as monoterpenes, limonene, etc.) on radical chemistry cannot be ignored (Ma et al., 2022; Wang et al., 2022b). k_{OVOCs} are categorized into three groups: $k_{OVOCs(Obs)}$, $k_{OVOCs(Model)}$, and k_{HCHO} . Given the significance of formaldehyde photolysis, the contribution of HCHO to k_{OVOCs} is distinguished. $k_{OVOCs(Obs)}$ encompasses species observed in addition to formaldehyde, such as acetaldehyde (ACD) and the oxidation products of isoprene (MACR and MVK). Intermediates generated by the model, including glyoxal (GLY), methylglyoxal (MGLY), higher aldehydes (ALD), ketones (KET), methyl ethyl ketone (MEK), and methanol (MOH), are classified as $k_{OVOCs(Model)}$. Upon considering $k_{OVOCs(Model)}$ calculated by RACM2-LIM1 mechanism, the reactivity calculated prior to September 10th aligns quite well with the observed OH reactivity.



349

350
351

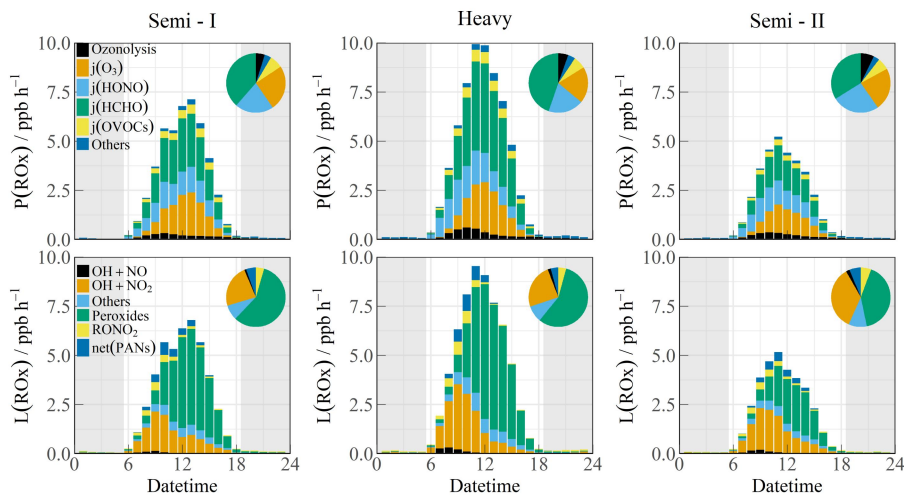
Fig. 4. Timeseries of the observed and modelled parameters for OH, HO₂ and k_{OH} during the observation period. (a) OH, (b) HO₂, (c) k_{OH} .

352 The significant variations in oxidation can be inferred from the disparities during
353 different pollution periods (Fig. S5). During Semi I, there was a good agreement between
354 the measurement and model for peroxy radicals during the daytime. The RACM2-LIM1
355 mechanism effectively replicated the morning OH radical concentration. However,
356 following 10:00, NO gradually declined, and the increasing OH concentration could not
357 be accounted for by the HO_2+NO formation channel, resulting in a maximum
358 underestimation of $5.85\times 10^6 \text{ cm}^{-3}$ (Hofzumahaus et al., 2009; Lu et al., 2012). In the
359 Semi II episode, OH was not underestimated in the low-NO regime, with a slight
360 overestimation of HO_2 concentration. However, the simulated RO_2 concentration was
361 only $3.78\times 10^8 \text{ cm}^{-3}$, whereas observations were 2.77 times larger than the simulation,
362 indicating the existence of additional reaction pathways that likely propagated the
363 $\text{OH}\rightarrow\text{RO}_2$ conversion efficiency. A significant discrepancy of radicals existed in the
364 heavy ozone concentration, with OH, HO_2 , and RO_2 radicals concurrently underestimated
365 at noon by $8.23\times 10^6 \text{ cm}^{-3}$, $3.94\times 10^8 \text{ cm}^{-3}$ and $11.59\times 10^8 \text{ cm}^{-3}$, respectively. The observed
366 HO_2/RO_2 ratio approached 1:1, while the model reflected an unreasonable ratio of 3:1,
367 indicating deficiencies in both primary sources and secondary propagation. The
368 calculated reactivity seems to compare well with the observed OH reactivity at the start
369 of the measurement period, but then there is evidence of missing OH reactivity after
370 September 10th (Fig. 4(d)). Due to the limitations of available instruments, this
371 observation only measured a limited number of OVOCs species, making it difficult to
372 accurately quantify the contribution of larger aldehydes and ketones, carboxylic acids,
373 nitrophenols, and other multifunctional species to k_{OH} (Wang et al., 2024). Since the
374 MCM mechanism considers more secondary formation reactions than the RACM2
375 mechanism, it can qualitatively assess the photochemical role of unmeasured OVOCs
376 species in the atmosphere (Wang et al., 2022d). The additional modeled OVOCs by the
377 MCM v3.3.1 mechanism contributed $\sim 2.4 \text{ s}^{-1}$ to the missing OH reactivity (Fig. S6).
378 During Heavy period, the reactivity of more model oxidation products increased the
379 daytime k_{OH} by about 5.1 s^{-1} . Therefore, the observed k_{OH} can serve as an upper limit for
380 sensitivity tests, thereby the full suite of radical measurement can be performed to
381 explore the missing oxidation properties and ozone formation (Section 4.1).

382 Fig. 5 displays the diurnal profiles of the ROx budget during different episodes. In

383 Semi I, formaldehyde photolysis showed a higher contribution (38.6%), while HONO
 384 photolysis (21.0%) and ozone photolysis (24.7%) accounted for similar proportions in
 385 primary sources. The contribution of photolysis from other OVOCs was comparable to
 386 that of ozonolysis reactions (7.2% vs. 4.8%). However, in Semi II, the decreased
 387 oxidation level was attributed to lower ROx sources, despite the similar proportions.
 388 During the Heavy period, the primary sources dramatically increased (up to ~10 ppb/h),
 389 with HCHO photolysis contributing the most, alongside other sources at common levels
 390 (ranging between 1.74 – 2.66 ppb/h) in the YRD region (Ma et al., 2022). Fast HCHO
 391 oxidation dominated the radical primary source during heavy ozone pollution, which
 392 contrasts with the dominant role of HONO/O₃ in other megacities (Yang et al., 2022; Tan
 393 et al., 2017b; Yang et al., 2021a).

394 The radical removal rate during the daytime was generally balanced with production
 395 contributions. In the morning, owing to high NOx concentrations, radical termination was
 396 mainly dominated by OH+NO₂, OH+NO, RO₂+NO, and RO₂+NO₂. Furthermore, the
 397 formation of peroxy nitrate accounted for a certain proportion (~5%). As NOx
 398 concentrations decreased after 10:00, self-reactions in peroxy radicals became significant.



399
 400 **Fig. 5.** The diurnal profiles of ROx budget during different polluted episodes (Semi I, Heavy, and Semi II). The
 401 pie chart denotes proportions in different parts during the daytime (10:00-15:00). The grey areas denote nighttime.
 402

403 By comparing the known sources and sinks for radicals, unknown processes for
 404 initiation, transformation and termination can be determined in the experimental budget
 405 analysis (Fig. S7). During the Semi I period, the production and destruction rates of HO₂,
 406 RO₂, and total ROx radicals were very consistent, but a significant lack of a source term
 407 for OH radicals was existed after 10:00. This missing source became more pronounced

407 during the Heavy period, reaching 16 ppb/h at noon, which is close to the results
408 observed by APHH, but three times that observed by Heshan in PRD region(Tan et al.,
409 2019b; Whalley et al., 2021). The ratio of OH production-to-destruction rate during the
410 Semi II period was close to 1, indicating consistency between the observed results of OH,
411 HO_2 , k_{OH} , and other precursors(Whalley et al., 2018). However, the generation of HO_2
412 radicals in the morning was about twice as high as the removal rate, suggesting that there
413 are contributions from unconsidered HO_2 radical removal channels (such as
414 heterogeneous reactions)(Song et al., 2021). During the Heavy period, there was a rapid
415 total removal rate of RO_2 radicals, reflecting the dominated HO_2 generation by the
416 reaction of RO_2 radicals with NO. Although the P(HO_2) and D(HO_2) were quite in
417 balance, the removal rate of RO_2 radicals far exceeded the known production rate
418 (especially before 12:00). Previous work has shown that halogen chemistry (such as
419 photolysis of nitryl chloride (ClNO_2)) could be an important source in the morning time,
420 but this was not included in the calculation of ROx or RO_2 budget in this campaign(Tan
421 et al., 2017b). The steady-state analysis for HO_2 radical in the London campaign
422 emphasized that only by significantly reducing the observed RO_2 -to- HO_2 propagation
423 rate to just 15% could balance both P(HO_2) and D(HO_2), indicating that the RO_2 -related
424 mechanism for propagation to other radical species may not be fully understood(Whalley
425 et al., 2018). Therefore, based on the current knowledge seems unlikely to explain the
426 required source-sink difference of nearly 25 ppb/h in the RO_2 budget. Sensitivity analysis
427 is needed to further infer the causes of the difference for the experimental budget
428 analysis.

429 **3.3 Oxidation comparison**

430 The concentration of OH radicals during the daytime is a crucial indicator of
431 atmospheric oxidation levels (Liu et al., 2021). Table 2 summarized radicals and related
432 parameters for regions with similar latitudes ($32.0^\circ \pm 2^\circ \text{ N}$, $j(\text{O}^1\text{D}) \approx 2.5 \pm 0.5 \times 10^{-5} \text{ s}^{-1}$).
433 The joint influence of solar radiation and local photochemistry resulted in megacities
434 exhibiting intense oxidation levels in summer/autumn, characterized by OH radicals
435 being maintained at approximately $10.0 \times 10^6 \text{ cm}^{-3}$ at noon. Notably, an observation in
436 Houston revealed an OH concentration of nearly $20.0 \times 10^6 \text{ cm}^{-3}$, with k_{OH} of 10 s^{-1} (Mao
437 et al., 2010). In areas such as Los Angeles, Pasadena, and Tokyo, the propagation

438 efficiency of radicals was restricted due to fresh anthropogenic emissions. OH
 439 concentrations were only half of those observed in other megacities, with higher
 440 inorganic-dominated k_{OH} recorded (Pasadena, $\sim 20 \text{ s}^{-1}$) (George et al., 1999; Griffith et al.,
 441 2016; Yugo Kanaya et al., 2007). In the TROPSTECT observation, the observed k_{OH}
 442 exceeded the mean value at the same latitude ($> 15 \text{ s}^{-1}$). Additionally, during the Heavy
 443 episode, higher OH concentration ($13.5 \times 10^6 \text{ cm}^{-3}$) was found, comparable to the highest
 444 level at regions with similar latitude (Houston 2000/2006, (Mao et al., 2010)).
 445 Synchronous elevation in radical concentration and reactivity indicated a strong oxidation
 446 level in the YRD region.

447 The observations in the YRD region showed a stable conversion factor ($\text{OH} \cdot j(\text{O}^1\text{D})$)
 448 of $4 \pm 1 \times 10^{11} \text{ cm}^{-3} \text{ s}$, which was comparable to other megacities in the PRD, NCP, and
 449 SCB regions (Ma et al., 2022; Tan et al., 2019a). The corresponding slope between OH
 450 concentration and solar radiation was used to quantify the oxidation efficiency from
 451 photolysis, and it was observed that a higher slope of $5.3 \times 10^{11} \text{ cm}^{-3} \text{ s}$ during the Heavy
 452 period indicated an active radical chemistry. This implies that there is a strong oxidation
 453 efficiency from photolysis in the YRD region.

454 During summer and autumn seasons, photochemical pollution is a common
 455 occurrence, as noted by (Tan et al., 2021). Analysis of radical concentration across
 456 different regions reveals that the YRD region exhibited concentrations higher than 10^7
 457 cm^{-3} , slightly lower than in Guangzhou in 2006 but consistent with observations in other
 458 megacities (Ma et al., 2022; Tan et al., 2017a; Lu et al., 2012; Yang et al., 2021a).
 459 Conversely, winter is characterized by haze pollution (Ma et al., 2019). An urban site in
 460 Shanghai reported a peak OH concentration of $2.6 \times 10^6 \text{ cm}^{-3}$, closely resembling the $1.7 -$
 461 $3.1 \times 10^6 \text{ cm}^{-3}$ range found in polluted winter atmospheres (Zhang et al., 2022a). Although
 462 no significant regional disparities in oxidation levels were detected in agglomerations,
 463 attention should be directed to the YRD region due to its elevated radical concentration,
 464 reactivity, and photolysis efficiency, signaling the need to investigate its role in radical
 465 chemistry.

466 **Table 2.** Summary of radical concentrations and related species concentrations at regions with similar latitude and
 467 megapolitan areas in China. All data are listed as the average in noontime (11:00~13:00).

Location	Latitude	Year	OH (10^6 cm^{-3})	k_{OH} (s^{-1})	$j(\text{O}^1\text{D})$ (10^{-5} s^{-1})	Slope ($10^{11} \text{ cm}^{-3} \text{ s}$)	References
Regions with similar latitude							
Los Angeles	34.1° N	Sep 1993	6.0	-	-	-	(George et al., 1999)

Nashville	36.2° N	Jun–Jul 1999	10.0	10.2	3.0	3.3 ^c	(Martinez et al., 2003)
Houston	29.7° N	Aug 2000	20.0	9.0 ^b	3.0	6.7 ^c	(Mao et al., 2010)
Tokyo	35.6° N	Jul–Aug 2004	6.3	-	2.5	3.0	(Yugo Kanaya et al., 2007)
Houston	29.7° N	Sep 2006	15.0	11.0	3.1	5.0 ^c	(Mao et al., 2010)
Pasadena	34.1° N	May–Jun 2010	4.0	20.0	2.5	1.6 ^c	(Griffith et al., 2016)
Taizhou	32.6° N	May–Jun 2018	10.6	10.8 ^a	2.1	4.8	(Ma et al., 2022)
Chengdu	30.7° N	Aug 2019	10.0	8.0	2.2	4.1	(Yang et al., 2021a)
TROPSTECT (Heavy)	31.9° N	Sep 2020	13.5	16.0	2.6	5.3	This work
TROPSTECT (Semi)	31.9° N	Sep 2020	7.2	14.2	2.4	3.1	This work
Regions in megapolitan areas in China							
Guangzhou (PRD)	23.5° N	Jul 2006	12.6	17.9	3.5 ^b	4.5	(Lu et al., 2012)
Wangdu (NCP)	38.7° N	Jun–Jul 2014	8.3	15.0	1.8	4.5	(Tan et al., 2017b)
Beijing (NCP)	39.9° N	May–Jun 2017	9.0	30.0	2.4	3.8 ^c	(Whalley et al., 2021)
Taizhou (YRD)	32.6° N	May–Jun 2018	10.6	10.8 ^a	2.1	4.8	(Ma et al., 2022)
Shenzhen (PRD)	22.6° N	Sep–Oct 2018	4.5	21.0	1.8	2.4	(Yang et al., 2022)
Chengdu (SCB)	30.7° N	Aug 2019	9.0	8.0	2.2	4.0	(Yang et al., 2021a)
Hefei (YRD)	31.9° N	Sep 2020	10.4	14.3	2.4	4.4	This work

468 ^a The modeled k_{OH} .

469 ^b Value only in the afternoon.

470 ^c Using the ratio of OH / $j(O^1D)$

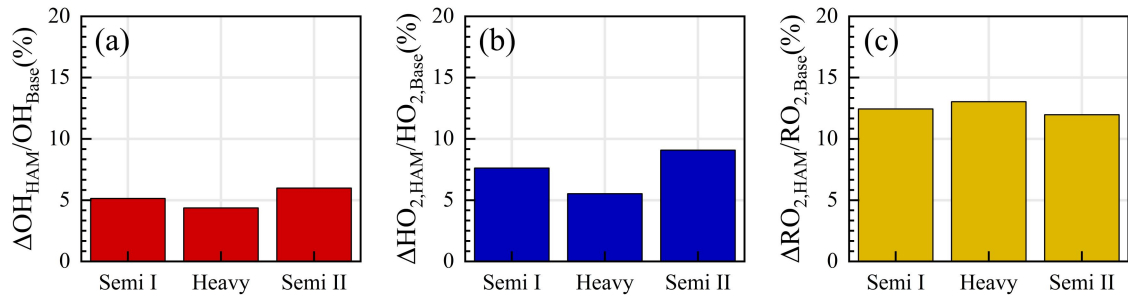
4 Discussion

4.1 Measurement–model reconciliation for radicals

4.1.1 OH underestimation

471 Full suite of OH, HO₂, RO₂ and k_{OH} was utilized in the TROPSTECT campaign to
472 untangle a thorough understanding of oxidation mechanisms where base model failed.
473 One specific phenomenon was the absence of an OH source in situations where NO
474 levels gradually decreased after 10:00. Missing OH sources are closely related to the
475 chemistry of OVOCs(Yang et al., 2024a; Qu et al., 2021). Reactive aldehyde chemistry,
476 particularly the autoxidation of carbonyl organic peroxy radicals (R(CO)O₂) derived from
477 higher aldehydes, is a significant OH regeneration mechanism that has been shown to
478 contribute importantly to OH sources in regions with abundant natural and anthropogenic
479 emissions during warm seasons(Yang et al., 2024b). In this study, the higher aldehyde
480 mechanism (HAM) by Yang et al was parameterized into the base model to test new
481 insights into the potential missing radical chemistry (Fig. 6). The results indicate that the
482 contribution of the HAM mechanism to OH radicals in different episodes ranged between
483

486 4.4% - 6.0% (Fig. 6(a)). The additional HAM mechanism seems to have a small effect on
 487 the measured OH radical concentration. Thus, an empirical hypothesis is proposed in the
 488 'HAM+4ALD on' scenario to increase the concentration of higher-order aldehydes by
 489 approximately fourfold, thereby replicating the effect of missing OVOCs sources on
 490 radicals. Detailed description is presented in Section 4.3.



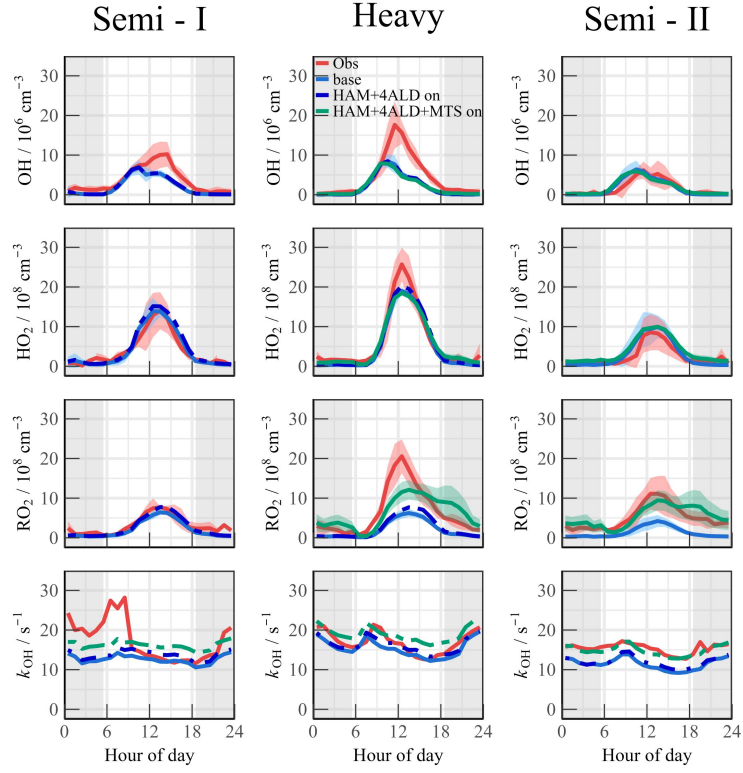
491
 492 **Fig. 6.** The response of (a) OH, (b) HO₂ and (c) RO₂ radicals to the Higher Aldehyde Mechanism (HAM) in
 493 different episodes (Semi I, Heavy, and Semi II) in diurnal time (10:00-15:00).

494 4.1.2 RO₂ underestimation

495 The base scenario in Semi II is capable of accurately reproducing the concentrations
 496 of OH and HO₂ radicals within the data uncertainty. However, the simulated RO₂
 497 concentration by the base model is only $3.78 \times 10^8 \text{ cm}^{-3}$, which does not align with the
 498 observed oxidation levels in YRD, indicating a clear discrepancy. This underestimation is
 499 similarly evident in the APHH observation in Beijing, as the highest observed
 500 concentration of RO₂ radicals reached $5.5 \times 10^9 \text{ cm}^{-3}$, far exceeding the level predicted by
 501 the MCM v3.3.1 mechanism (Whalley et al., 2021). The failure to reproduce the RO₂
 502 concentration reflects the inadequacy of the mechanisms related to RO₂ radicals due to
 503 diverse oxidation reactions. This issue is further elucidated by previous studies, which
 504 highlighted the possibility of certain VOCs undergoing more intricate isomerization or
 505 fragmentation steps to sustain the long lifetime of RO₂ radicals (Whalley et al., 2018;
 506 Whalley et al., 2021). Higher aldehyde chemistry is a concrete manifestation of verifying
 507 the aforementioned hypothesis for RO₂ sources (Yang et al., 2024b). The autoxidation
 508 process of R(CO)O₂, encompasses a hydrogen migration process that transforms it into
 509 the ·OOR(CO)OOH radical (Wang et al., 2019b). This radical subsequently reacts with
 510 NO to yield the ·OR(CO)OOH radical. The ·OR(CO)OOH radical predominantly
 511 undergoes two successive rapid hydrogen migration reactions, ultimately resulting in the
 512 formation of HO₂ radicals and hydroperoxy carbonyl (HPC). Consequently, the HAM

513 mechanism extends the lifetime of the RO₂ radical, providing a valuable complement to
514 the unaccounted sources of RO₂ radicals. As depicted in Fig. 6, the incorporation of the
515 HAM mechanism results in an approximate 7.4% and 12.5% increase in the
516 concentrations of HO₂ and RO₂ radicals, respectively.

517 It is important to note that the total concentrations of primary emitted aldehydes and
518 the HPC group may be underestimated, which could lead to the aforementioned analysis
519 being conservative in nature. The union of k_{OH} and RO₂ measurement can help reveal the
520 magnitude of missing RO₂ as a hypothesis of sensitivity analysis. Discrepancy of OH
521 reactivity ($\sim 3 - 5 \text{ s}^{-1}$) between measurement and model suggested that an additional
522 driving force was necessary to complete the OH to RO₂ step. Approximately 0.4 ppb of
523 monoterpenes are introduced as chemical reactions of complex alkoxy radicals, which are
524 consistent with atmospheric level and can better reconcile the missing k_{OH} between
525 observation and simulation (Fig. 7) (Wang et al., 2022b). The RACM2 mechanism
526 identified α -pinene (API) and limonene (LIM) as representative of monoterpenes, and the
527 mean of the species was considered the average effect of monoterpenes chemistry (the
528 green line in Fig. 7). The 'HAM +4ALD+MTS on' scenario can reasonably reproduce the
529 measured reactivity, and the chemistry of peroxy radicals in Semi II was reasonably
530 described by introducing the source of complex alkoxy radicals, decreasing the
531 obs-to-mod ratio from 2.2 to 1.3. Furthermore, the introduction of additional complex
532 alkoxy radicals had minimal impact on HO_x chemistry, with changes in daytime OH and
533 HO₂ concentrations of less than $5 \times 10^5 \text{ cm}^{-3}$ and $2.5 \times 10^7 \text{ cm}^{-3}$, respectively. This
534 demonstrates the robustness of HO_x radical in response to potential monoterpane.



535

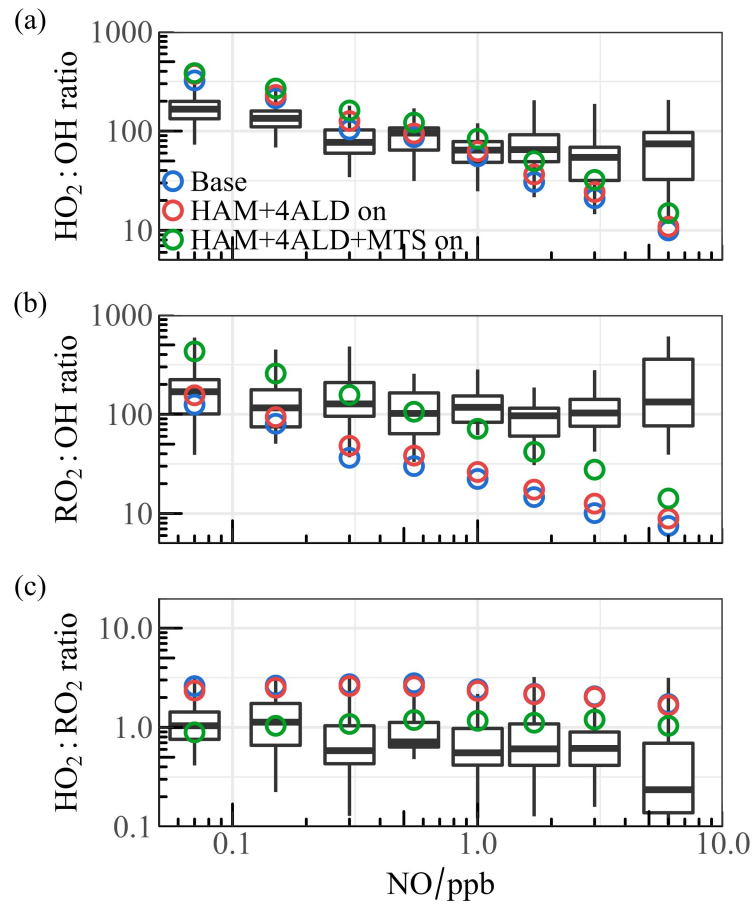
536
537

Fig. 7. The mean diurnal profiles of measured and modeled OH, HO₂, RO₂ and k_{OH} at different scenarios. The grey areas denote nighttime.

538 4.2 Effect of mechanism reconciliation on oxidation

539 Upon completing the hypothetical investigation into the radical underestimation,
 540 both radical concentration and oxidation coordinating deficiency are worthy of examine
 541 (Fig. S8). To eliminate the influence of non-photolytic processes, only the daytime
 542 concentration range with $j(O^1D)$ greater than $5 \times 10^{-6} \text{ s}^{-1}$ was selected. The boxplots
 543 illustrate the ratio of observation to simulation (base model), with the circles representing
 544 the average values after integrating different mechanisms into the base scenario. In the
 545 low NO regime (NO < 1 ppb), the OH underestimation was consistently prominent as NO
 546 concentration decreased, and the base model was able to reasonably reflect the HO₂
 547 distribution contrastly. As NO levels increased, the simulated OH concentration aligned
 548 well with the observation, but both HO₂ and RO₂ concentrations exhibited
 549 underprediction. RO₂ underestimation extended across the entire NO range, and could
 550 rise to over 10 times when NO levels reached about 10 ppb. Sensitivity tests based on the
 551 full suite of radical measurement revealed that the introduction of larger RO₂ alleviated
 552 the absence of certain sources by 2 to 4 times.

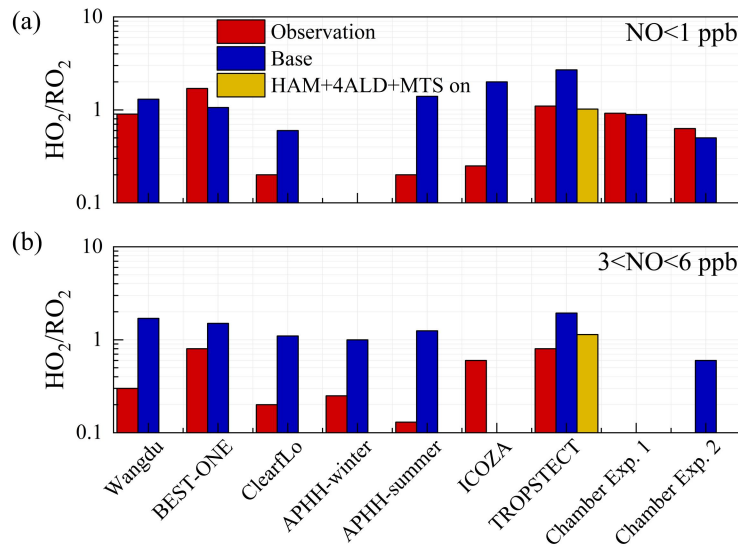
553 The coordinate ratios of radical serves as another test for ROx propagation (Fig. 8).
554 The observed HO₂/OH ratio is approximately 100, declining to some extent as the
555 concentration of NO increases, which is consistent with previous studies (Griffith et al.,
556 2016; Griffith et al., 2013). However, the base model does not accurately replicate the
557 curve depicting the change in HO₂/OH ratio, as shown in Fig. 8 (a). At low NO levels, the
558 ratio significantly overestimated and shows a steeper decline compared to the base
559 scenario as NO levels increase. Furthermore, the observed RO₂/OH ratios remain around
560 100, whereas the predicted values are significantly underestimated when NO exceeds 1
561 ppb (refer to Fig. 8(b)). In terms of the observed HO₂/RO₂ ratio, it maintains a relatively
562 constant trend within the range of 0.5 – 1.5, while the model overestimated by more than
563 twice, highlighting an inconsistency between the conversion of RO₂→HO₂. The
564 incorporation of the HAM mechanism has proven to slightly balance the HO₂/OH ratio as
565 illustrated in Fig. 8(a), and altered the coordination between RO₂ and OH across the
566 entire NO range (Fig. 8(b)). The larger RO₂ isomerization associated with HAM
567 mechanism in chemically complex environments is key to fully understanding
568 tropospheric chemistry, and a better coordination of HO₂/OH, RO₂/OH, and HO₂/RO₂
569 ratios are established by incorporating additional mechanisms.



570
 571 **Fig. 8.** The ratios for (a) HO_2/OH , (b) RO_2/OH , and (c) HO_2/RO_2 show a correlation with NO levels. Boxplot
 572 diagrams are used to illustrate the minimum, 25th percentile, median, 75th percentile, and maximum values of the
 573 observed dataset. The circles represent the median values for the base model as well as for different mechanisms added
 574 to the model within various ranges.

575 The HO_2/RO_2 parameter was utilized to explore the transformation relationship
 576 between HO_2 and RO_2 radicals. If HO_2 is formed from an RO_2 radical, it would result in
 577 an HO_2/RO_2 radical concentration ratio of approximately 1. The HO_2/RO_2 ratios derived
 578 from radical concentrations measured by laser-induced fluorescence instruments and
 579 calculated using the MCM or RACM models were summarized in Fig. 9. In field studies,
 580 the observed HO_2/RO_2 ratios were between 0.2 - 1.7 under low-NO conditions ($\text{NO} < 1$
 581 ppb) and only 0.1 - 0.8 under high-NO conditions ($3 < \text{NO} < 6$ ppb). From the
 582 perspective of model-observation matching, except for three measurements in ClearfLo,
 583 ICOZA and APHH-summer campaigns, the HO_2/RO_2 ratios in other regions could be
 584 reasonably reflected by the MCM or RACM2 mechanisms(Woodward-Massey et al.,
 585 2023; Whalley et al., 2021; Whalley et al., 2018; Färber et al., 2024). However, the ratio
 586 is generally underestimated under high NO conditions, reaching up to 5 times in ClearfLo.

587 According to the latest chamber experiments, the HO₂/RO₂ radical concentration ratios
 588 for VOCs forming HO₂ are 0.6 for both one-step and two-step reactions. Therefore, the
 589 extremely low HO₂/RO₂ ratios observed in field campaigns can only be explained if
 590 almost all RO₂ radicals undergo multiple-step reactions before forming HO₂. During the
 591 TROPSTECT campaign, the observed HO₂/RO₂ remains at 1.1 and 0.8 under low-NO
 592 and high-NO conditions, respectively. After considering the sources of complex alkoxy
 593 radicals in the 'HAM +4ALD+MTS on' scenario, the simulated values of HO₂/RO₂ in
 594 both low-NO and high-NO regions match the observed values well.



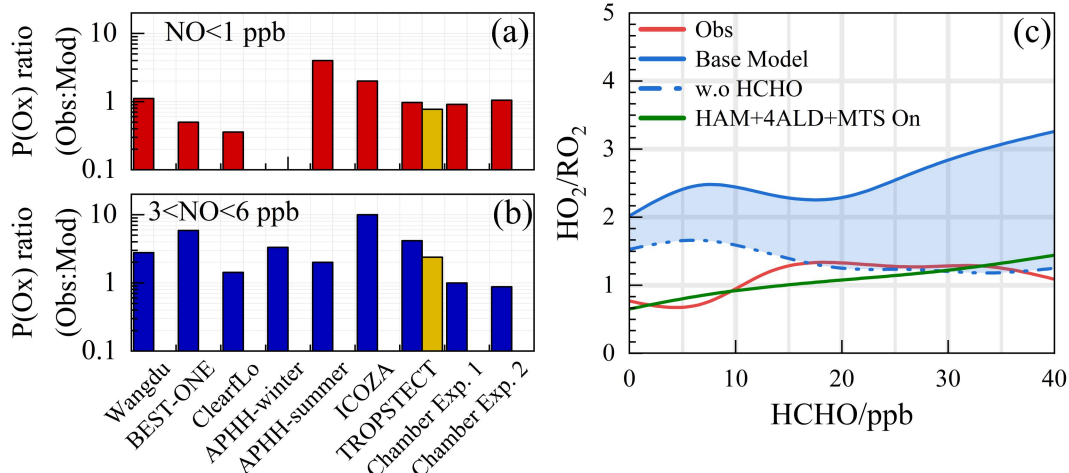
595

596 **Fig. 9.** Summary of the HO₂/RO₂ ratios derived from radical concentrations measured by laser-induced fluorescence
 597 instruments and calculated using the MCM or RACM models under (a) low-NO and (b) high-NO conditions.
 598 Charmer Exp. 1 and Charmer Exp. 2 denotes the parameters by single-step HO₂ formation and multi-step HO₂
 599 formation determined in the chamber by (Färber et al., 2024).

600 4.3 Missing OVOCs sources influence ozone production

601 The consistency between model predictions and observed measurements for ozone
 602 production, akin to the concentration ratio of HO₂/RO₂, is depicted in Fig. 10(a)(b). In
 603 areas with low NO levels, the ratio of modeled to actual ozone production ranges from
 604 0.5 to 2, with the exception of the ClearfLo and APHH-summer
 605 datasets(Woodward-Massey et al., 2023; Whalley et al., 2021). Conversely, under high
 606 NO conditions (with NO concentrations between 3 and 6 ppbv), the ozone production
 607 rate (P(O_x)) derived from measured radical concentrations typically exceeds that of the
 608 base model's predictions by more than threefold. Laboratory experiments focusing on the
 609 oxidation of representative VOCs suggest that ozone production can be enhanced by

610 approximately 25% for the anthropogenic VOCs under investigation (Färber et al., 2024).



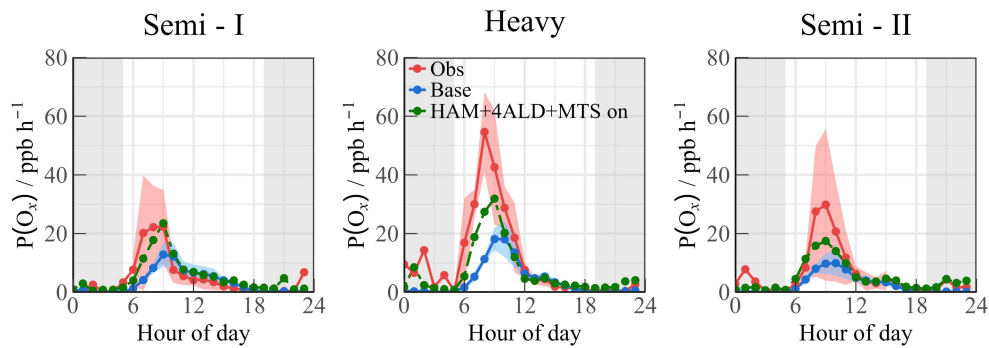
611

612 **Fig. 10.** Summary of the $P(Ox)_{\text{Obs}}/P(Ox)_{\text{Mod}}$ under **(a)** low-NO and **(b)** high-NO conditions. The yellow bar chart
 613 represents the simulation scenario of 'HAM +4ALD+MTS on'. **(c)** The ratios for HO_2/RO_2 show a correlation with
 614 HCHO levels. The blue shading represents the range of variation from constrained to unconstrained formaldehyde
 615 conditions. Chamber Exp. 1 and Chamber Exp. 2 denotes the parameters by single-step HO_2 formation and multi-step
 616 HO_2 formation determined in the chamber by (Färber et al., 2024).

617 The reasons for the discrepancy between simulated and observed values for ozone
 618 production deserve further investigation. As depicted in Fig. 10(c), the simulated
 619 HO₂/RO₂ ratios display a robust positive correlation with photochemical activity,
 620 fluctuating between 2 and 4. A notable feature during severe ozone pollution is the
 621 intense distribution of formaldehyde, with an average concentration of 21.81 ± 4.57 ppb
 622 (11:00 – 13:00). While formaldehyde acts as a precursor for HO₂ radicals, it does not
 623 directly generate RO₂ radicals. The contributions of OVOCs to the RO₂ radical do not
 624 exhibit the same intensity as formaldehyde, and the current mechanism encounters
 625 difficulties in replicating formaldehyde concentrations (Fig. S9). The simulation of
 626 formaldehyde concentrations using the MCM v3.3.1 mechanism has shown improvement,
 627 indicating that the secondary formation of unmeasured species, such as OVOCs, will
 628 feedback on RO₂ radical levels. When formaldehyde levels are unconstrained, the
 629 simulated HO₂/RO₂ ratios align with observations, suggesting that under the prevailing
 630 chemical mechanism, the photochemical efficiency of formaldehyde and other OVOCs is
 631 similar. Therefore, an empirical hypothesis is proposed to amplify the concentration of
 632 higher-order aldehydes by a factor of about 4, which is the proportion of formaldehyde
 633 concentration underestimated by the model. The qualitative assessment of the impact of
 634 missing aldehyde primary emissions on RO₂ radical concentrations was combined with

635 the HAM mechanism across the entire photochemical spectrum (Fig. S10). Enhanced
 636 impact of aldehyde autoxidation in the presence of weak photochemical conditions could
 637 alter the simulated levels of OH and HO₂ radicals by approximately 13.9% and 18.1%,
 638 respectively. However, higher ALD concentrations will be achieved under intensive
 639 photochemical conditions, leading to the gradual dominance of the sink channels for OH
 640 + OVOCs, with the effect of autoxidation mechanisms gradually decreasing. RO₂ radical
 641 concentrations is notably more sensitive to the HAM mechanism, where incorporates
 642 additional OVOCs, can enhance the simulation of RO₂ radical concentrations by 20 -
 643 40%.

644 On the basis of HAM mechanism, the 'HAM +4ALD+MTS on' scenario represents
 645 an effort to enhance the congruence between modeled and measured radical
 646 concentrations. In Fig. S11, with increasing NO concentration, the overall P(O_x)
 647 amplified, reaching a maximum of approximately 30 ppb/h. However, the imperfect
 648 understanding of the mechanisms related to peroxy radicals ultimately leads to
 649 misjudgment of the ozone production process in high NO regimes, with a degree of
 650 underestimation close to 10 times, as illustrated in Fig. S11(b). Notably, the deficiency in
 651 the ozone generation mechanism was adequately explained within a certain range in the
 652 'HAM +4ALD+MTS on' scenario, leading to an enhancement in the simulation
 653 performance of P(O_x) in the high NO_x region. The incorporation of OVOCs and larger
 654 alkoxy radicals derived from monoterpenes has refined the model-measurement
 655 agreement for ozone formation under high NO conditions, reducing the discrepancy from
 656 4.17 to 2.39 (Fig. 11).



657
 658 **Fig. 11.** The P(O_x) values that calculated by radical values under different scenarios. The grey areas denote
 659 nighttime.

660 Therefore, reasonable simulation of the concentration of peroxy radicals is key to

661 accurately quantifying the process of ozone generation. Although limiting formaldehyde
662 can partially offset the HO₂ radical cycle and enhance the precision of HO_x radical
663 chemistry studies, additional measurements should be undertaken for other OVOCs,
664 coupled with the deployment of full-chain radical detection systems, to accurately
665 elucidate the oxidation processes under severe ozone pollution conditions.

666 **5 Conclusion**

667 The full suite radical measurement of OH, HO₂, RO₂ and k_{OH} was first deployed in
668 the YRD region (TROPSTECT) and encountered with a prolonged ozone pollution in
669 September 2020. The diurnal peaks of radicals exhibited considerable variation due to
670 environmental factors, showing ranges of 3.6 to 27.1×10^6 cm⁻³ for OH, 2.1 to 33.2×10^8
671 cm⁻³ for HO₂, and 4.9 to 30.5×10^8 cm⁻³ for RO₂. Continuous k_{OH} data fell within a range
672 of 8.6 – 30.2 s⁻¹, demonstrating the dominant behavior of organic species in diurnal
673 reactivity. Furthermore, observations in the YRD region were found to be similar to those
674 in other megacities, suggesting no significant regional differences in oxidation levels
675 were observed in agglomerations overall.

676 At a heavy ozone pollution episode, the oxidation level reached intensive compared
677 with other sites, and the simulated OH, HO₂, and RO₂ radicals provided by the
678 RACM2-LIM1 mechanism failed to adequately match the observed data both in radical
679 concentration and experimental radical budget. Sensitivity tests based on the full suite of
680 radical measurement revealed that the HAM mechanism effectively complements the
681 non-traditional regeneration of OH radicals, improving by 4.4% - 6.0% compared to the
682 base scenario, while the concentrations of HO₂ and RO₂ radicals increased by
683 approximately 7.4% and 12.5%, respectively. Under the constraints of k_{OH} measurement,
684 the inclusion of OVOCs and larger alkoxy radicals derived from monoterpenes enabled
685 better coordination of HO₂/OH, RO₂/OH, and HO₂/RO₂ ratios, and adequately improved
686 the model-measurement consistency for ozone formation, reducing the discrepancy under
687 high NO conditions from 4.17 to 2.39. This study enabled a deeper understanding of the
688 tropospheric radical chemistry at play. Notably,

689 ✓ A full suite of radical measurement can untangle the gap-bridge for the base model in
690 more chemically-complex environments as an hypothesis of sensitivity tests.

691 ✓ Additional measurements targeting more OVOCs should also be conducted to fulfill
692 the RO₂-related imbalance, and then accurately elucidating the oxidation under
693 severe ozone pollution.

694

695 **Financial support**

696 This work was supported by the National Key R&D Program of China
697 (2022YFC3700301), the National Natural Science Foundation of China (62275250,
698 U19A2044, 42030609), the Natural Science Foundation of Anhui Province (No.
699 2008085J20), the Anhui Provincial Key R&D Program (2022l07020022), and the
700 Distinguished Program of Jianghuai Talents Program of Excellence (HYRCSTZ202401).

701 **Data availability**

702 The data used in this study are available upon request (rzhu@aiofm.ac.cn).

703 **Author contributions**

704 WQ Liu, PH Xie, RZ Hu contributed to the conception of this study. RZ Hu and GX
705 Zhang performed the data analyses and manuscript writing. All authors contributed to
706 measurements, discussed results, and commented on the paper.

707 **Competing interests**

708 The contact author has declared that none of the authors has any competing interests.
709

710 References

711 Duan, J., Qin, M., Ouyang, B., Fang, W., Li, X., Lu, K., Tang, K., Liang, S., Meng, F., Hu, Z., Xie, P., Liu,
712 W., and Häsler, R.: Development of an incoherent broadband cavity-enhanced absorption spectrometer for
713 in situ measurements of HONO and NO₂, *Atmos Meas Tech*, 11, 4531-4543, 10.5194/amt-11-4531-2018,
714 2018.

715 Färber, M., Fuchs, H., Bohn, B., Carlsson, P. T. M., Gkatzelis, G. I., Marcillo Lara, A. C., Rohrer, F.,
716 Vereecken, L., Wedel, S., Wahner, A., and Novelli, A.: Effect of the Alkoxy Radical Chemistry on the
717 Ozone Formation from Anthropogenic Organic Compounds Investigated in Chamber Experiments, *ACS*
718 *ES&T Air*, 1, 1096-1111, 10.1021/acsestairstair.4c00064, 2024.

719 Fuchs, H., Holland, F., and Hofzumahaus, A.: Measurement of tropospheric RO₂ and HO₂ radicals by a
720 laser-induced fluorescence instrument, *Rev of Sci Inst*, 79, 084104, 10.1063/1.2968712, 2008.

721 George, L. A., Hard, T. M., and O'Brien, R. J.: Measurement of free radicals OH and HO₂ in Los Angeles
722 smog, *J Geophys Res-Atmos*, 104, 11643-11655, 1999.

723 Griffith, S. M., Hansen, R. F., Dusanter, S., Stevens, P. S., Alaghmand, M., Bertman, S. B., Carroll, M. A.,
724 Erickson, M., Galloway, M., Grossberg, N., Hottle, J., Hou, J., Jobson, B. T., Kamprath, A., Keutsch, F. N.,
725 Lefer, B. L., Mielke, L. H., O'Brien, A., Shepson, P. B., Thurlow, M., Wallace, W., Zhang, N., and Zhou, X.
726 L.: OH and HO₂ radical chemistry during PROPHET 2008 and CABINEX 2009-Part 1: Measurements and
727 model comparison, *Atmos Chem Phys*, 13, 5403-5423, 10.5194/acp-13-5403-2013, 2013.

728 Griffith, S. M., Hansen, R. F., Dusanter, S., Michoud, V., Gilman, J. B., Kuster, W. C., Veres, P. R., Graus,
729 M., de Gouw, J. A., Roberts, J., Young, C., Washenfelder, R., Brown, S. S., Thalman, R., Waxman, E.,
730 Volkamer, R., Tsai, C., Stutz, J., Flynn, J. H., Grossberg, N., Lefer, B., Alvarez, S. L., Rappenglueck, B.,
731 Mielke, L. H., Osthoff, H. D., and Stevens, P. S.: Measurements of hydroxyl and hydroperoxy radicals
732 during CalNex-LA: Model comparisons and radical budgets, *J Geophys Res-Atmos*, 121, 4211-4232,
733 10.1002/2015jd024358, 2016.

734 Heard, D. E. and Pilling, M. J.: Measurement of OH and HO₂ in the troposphere, *Chemical reviews*, 103,
735 5163-5198, 10.1021/cr020522s, 2003.

736 Hofzumahaus, A., Rohrer, F., Lu, K., Bohn, B., Brauers, T., Chang, C.-C., Fuchs, H., Holland, F., Kita, K.,
737 Kondo, Y., Li, X., Lou, S., Shao, M., Zeng, L., Wahner, A., and Zhang, Y.: Amplified Trace Gas Removal in
738 the Troposphere, *Science*, 324, 1702-1704, 10.1126/science.1164566, 2009.

739 Hu, B., Duan, J., Hong, Y., Xu, L., Li, M., Bian, Y., Qin, M., Fang, W., Xie, P., and Chen, J.: Exploration of
740 the atmospheric chemistry of nitrous acid in a coastal city of southeastern China: results from
741 measurements across four seasons, *Atmos Chem Phys*, 22, 371-393, 10.5194/acp-22-371-2022, 2022.

742 Huang, J., Pan, X., Guo, X., and Li, G.: Health impact of China's Air Pollution Prevention and Control
743 Action Plan: an analysis of national air quality monitoring and mortality data, *Lancet Planet Health*, 2,
744 e313-e323, 10.1016/S2542-5196(18)30141-4, 2018.

745 Huang, X., Ding, A., Wang, Z., Ding, K., Gao, J., Chai, F., and Fu, C.: Amplified transboundary transport
746 of haze by aerosol-boundary layer interaction in China, *Nature Geoscience*, 13, 428-434,
747 10.1038/s41561-020-0583-4, 2020.

748 Jenkin, M. E., Saunders, S. M., and Pilling, M. J.: The tropospheric degradation of volatile organic
749 compounds: A protocol for mechanism development, *Atmos Environ*, 31, 81-104,
750 10.1016/s1352-2310(96)00105-7, 1997.

751 Jenkin, M. E., Saunders, S. M., Wagner, V., and Pilling, M. J.: Protocol for the development of the Master
752 Chemical Mechanism, MCM v3 (Part B): tropospheric degradation of aromatic volatile organic compounds,
753 *Atmos Chem Phys*, 3, 181-193, 10.5194/acp-3-181-2003, 2003.

754 Jia, W., Zhang, X., and Wang, Y.: Assessing the pollutant evolution mechanisms of heavy pollution
755 episodes in the Yangtze-Huaihe valley: A multiscale perspective, *Atmos Environ*, 244,
756 10.1016/j.atmosenv.2020.117986, 2021.

757 Kanaya, Y., Hofzumahaus, A., Dorn, H. P., Brauers, T., Fuchs, H., Holland, F., Rohrer, F., Bohn, B.,
758 Tillmann, R., Wegener, R., Wahner, A., Kajii, Y., Miyamoto, K., Nishida, S., Watanabe, K., Yoshino, A.,
759 Kubistin, D., Martinez, M., Rudolf, M., Harder, H., Berresheim, H., Elste, T., Plass-Duelmer, C., Stange, G.,
760 Kleffmann, J., Elshorbany, Y., and Schurath, U.: Comparisons of observed and modeled OH and HO₂
761 concentrations during the ambient measurement period of the HO(x)Comp field campaign, *Atmos Chem
762 Phys*, 12, 2567-2585, 10.5194/acp-12-2567-2012, 2012.

763 Levy, H.: Normal Atmosphere: Large Radical and Formaldehyde Concentrations Predicted, *Science*, 173,

764 141-143, 10.1126/science.173.3992.141, 1971.
765 Li, S., Lu, K., Ma, X., Yang, X., Chen, S., and Zhang, Y.: Field measurement of the organic peroxy radicals
766 by the low-pressure reactor plus laser-induced fluorescence spectroscopy, Chinese Chemical Letters, 31,
767 2799-2802, 10.1016/j.cclet.2020.07.051, 2020.
768 Liu, S., Li, X., Shen, X., Zeng, L., Huang, X., Zhu, B., Lin, L., and Lou, S.: Measurement and partition
769 analysis of atmospheric OH reactivity in autumn in Shenzhen, *Acta Scientiae Circumstantiae*, 39,
770 3600-3610, 2019.
771 Liu, Y., Li, J., Ma, Y., Zhou, M., Tan, Z., Zeng, L., Lu, K., and Zhang, Y.: A review of gas-phase chemical
772 mechanisms commonly used in atmospheric chemistry modelling, *Journal of Environmental Sciences*,
773 10.1016/j.jes.2022.10.031, 2022.
774 Liu, Z., Wang, Y., Hu, B., Lu, K., Tang, G., Ji, D., Yang, X., Gao, W., Xie, Y., Liu, J., Yao, D., Yang, Y., and
775 Zhang, Y.: Elucidating the quantitative characterization of atmospheric oxidation capacity in Beijing, China,
776 *Sci Total Environ*, 771, 10.1016/j.scitotenv.2021.145306, 2021.
777 Lou, S., Holland, F., Rohrer, F., Lu, K., Bohn, B., Brauers, T., Chang, C. C., Fuchs, H., Haseler, R., Kita, K.,
778 Kondo, Y., Li, X., Shao, M., Zeng, L., Wahner, A., Zhang, Y., Wang, W., and Hofzumahaus, A.:
779 Atmospheric OH reactivities in the Pearl River Delta – China in summer 2006: measurement and model
780 results, *Atmos Chem Phys*, 10, 11243–11260, 10.5194/acp-10-11243-2010, 2010.
781 Lu, K., Guo, S., Tan, Z., Wang, H., Shang, D., Liu, Y., Li, X., Wu, Z., Hu, M., and Zhang, Y.: Exploring
782 atmospheric free-radical chemistry in China: the self-cleansing capacity and the formation of secondary air
783 pollution, *Natl. Sci. Rev.*, 6, 579-594, 10.1093/nsr/nwy073, 2019a.
784 Lu, K. D., Guo, S., Tan, Z. F., Wang, H. C., Shang, D. J., Liu, Y. H., Li, X., Wu, Z. J., Hu, M., and Zhang, Y.
785 H.: Exploring atmospheric free-radical chemistry in China: the self-cleansing capacity and the formation of
786 secondary air pollution, *Natl. Sci. Rev.*, 6, 579-594, 10.1093/nsr/nwy073, 2019b.
787 Lu, K. D., Rohrer, F., Holland, F., Fuchs, H., Bohn, B., Brauers, T., Chang, C. C., Haeseler, R., Hu, M., Kita,
788 K., Kondo, Y., Li, X., Lou, S. R., Nehr, S., Shao, M., Zeng, L. M., Wahner, A., Zhang, Y. H., and
789 Hofzumahaus, A.: Observation and modelling of OH and HO₂ concentrations in the Pearl River Delta 2006:
790 a missing OH source in a VOC rich atmosphere, *Atmos Chem Phys*, 12, 1541-1569,
791 10.5194/acp-12-1541-2012, 2012.
792 Ma, X., Tan, Z., Lu, K., Yang, X., Chen, X., Wang, H., Chen, S., Fang, X., Li, S., Li, X., Liu, J., Liu, Y.,
793 Lou, S., Qiu, W., Wang, H., Zeng, L., and Zhang, Y.: OH and HO₂ radical chemistry at a suburban site
794 during the EXPLORE-YRD campaign in 2018, *Atmos Chem Phys*, 22, 7005-7028,
795 10.5194/acp-22-7005-2022, 2022.
796 Ma, X. F., Tan, Z. F., Lu, K. D., Yang, X. P., Liu, Y. H., Li, S. L., Li, X., Chen, S. Y., Novelli, A., Cho, C.
797 M., Zeng, L. M., Wahner, A., and Zhang, Y. H.: Winter photochemistry in Beijing: Observation and model
798 simulation of OH and HO₂ radicals at an urban site, *Sci Total Environ*, 685, 85-95,
799 10.1016/j.scitotenv.2019.05.329, 2019.
800 Mao, J., Ren, X., Chen, S., Brune, W. H., Chen, Z., Martinez, M., Harder, H., Lefer, B., Rappenglück, B.,
801 Flynn, J., and Leuchner, M.: Atmospheric oxidation capacity in the summer of Houston 2006: Comparison
802 with summer measurements in other metropolitan studies, *Atmos Environ*, 44, 4107-4115,
803 10.1016/j.atmosenv.2009.01.013, 2010.
804 Martinez, M., Harder, H., Kovacs, T. A., Simpas, J. B., Bassis, J., Lesher, R., Brune, W. H., Frost, G. J.,
805 Williams, E. J., Stroud, C. A., Jobson, B. T., Roberts, J. M., Hall, S. R., Shetter, R. E., Wert, B., Fried, A.,
806 Alicke, B., Stutz, J., Young, V. L., White, A. B., and Zamora, R. J.: OH and HO₂ concentrations, sources,
807 and loss rates during the Southern Oxidants Study in Nashville, Tennessee, summer 1999, *J Geophys
808 Res-Atmos*, 108, 10.1029/2003jd003551, 2003.
809 Peeters, J., Muller, J. F., Stavrakou, T., and Nguyen, V. S.: Hydroxyl Radical Recycling in Isoprene
810 Oxidation Driven by Hydrogen Bonding and Hydrogen Tunneling: The Upgraded LIM1 Mechanism, *J
811 Phys Chem A*, 118, 8625-8643, 10.1021/jp5033146, 2014.
812 Qu, H., Wang, Y., Zhang, R., Liu, X., Huey, L. G., Sjostedt, S., Zeng, L., Lu, K., Wu, Y., Shao, M., Hu, M.,
813 Tan, Z., Fuchs, H., Broch, S., Wahner, A., Zhu, T., and Zhang, Y.: Chemical Production of Oxygenated
814 Volatile Organic Compounds Strongly Enhances Boundary-Layer Oxidation Chemistry and Ozone
815 Production, *Environ Sci Technol*, 10.1021/acs.est.1c04489, 2021.
816 Ren, X., Olson, J. R., Crawford, J. H., Brune, W. H., Mao, J., Long, R. B., Chen, Z., Chen, G., Avery, M. A.,
817 Sachse, G. W., Barrick, J. D., Diskin, G. S., Huey, L. G., Fried, A., Cohen, R. C., Heikes, B., Wennberg, P.
818 O., Singh, H. B., Blake, D. R., and Shetter, R. E.: HO_x chemistry during INTEX-A 2004: Observation,
819 model calculation, and comparison with previous studies, *J Geophys Res-Atmos*, 113,

820 10.1029/2007jd009166, 2008.

821 Rohrer, F., Lu, K., Hofzumahaus, A., Bohn, B., Brauers, T., Chang, C.-C., Fuchs, H., Haeseler, R., Holland,
822 F., Hu, M., Kita, K., Kondo, Y., Li, X., Lou, S., Oebel, A., Shao, M., Zeng, L., Zhu, T., Zhang, Y., and
823 Wahner, A.: Maximum efficiency in the hydroxyl-radical-based self-cleansing of the troposphere, *Nature
824 Geoscience*, 7, 559-563, 10.1038/ngeo2199, 2014.

825 Shi, X., Ge, Y., Zheng, J., Ma, Y., Ren, X., and Zhang, Y.: Budget of nitrous acid and its impacts on
826 atmospheric oxidative capacity at an urban site in the central Yangtze River Delta region of China, *Atmos
827 Environ*, 238, 10.1016/j.atmosenv.2020.117725, 2020.

828 Slater, E. J., Whalley, L. K., Woodward-Massey, R., Ye, C., Lee, J. D., Squires, F., Hopkins, J. R., Dunmore,
829 R. E., Shaw, M., Hamilton, J. F., Lewis, A. C., Crilley, L. R., Kramer, L., Bloss, W., Vu, T., Sun, Y., Xu, W.,
830 Yue, S., Ren, L., Acton, W. J. F., Hewitt, C. N., Wang, X., Fu, P., and Heard, D. E.: Elevated levels of OH
831 observed in haze events during wintertime in central Beijing, *Atmos Chem Phys*, 20, 14847-14871,
832 10.5194/acp-20-14847-2020, 2020.

833 Song, H., Lu, K., Dong, H., Tan, Z., Chen, S., Zeng, L., and Zhang, Y.: Reduced Aerosol Uptake of
834 Hydroperoxyl Radical May Increase the Sensitivity of Ozone Production to Volatile Organic Compounds,
835 *Environmental Science & Technology Letters*, 9, 22-29, 10.1021/acs.estlett.1c00893, 2021.

836 Stockwell, W. R., Kirchner, F., Kuhn, M., and Seefeld, S.: A new mechanism for regional atmospheric
837 chemistry modeling, *J Geophys Res-Atmos*, 102, 25847-25879, 10.1029/97jd00849, 1997.

838 Stone, D., Whalley, L. K., and Heard, D. E.: Tropospheric OH and HO₂ radicals: field measurements and
839 model comparisons, *Chemical Society reviews*, 41, 6348-6404, 10.1039/c2cs35140d, 2012.

840 Tan, Z., Ma, X., Lu, K., Jiang, M., Zou, Q., Wang, H., Zeng, L., and Zhang, Y.: Direct evidence of local
841 photochemical production driven ozone episode in Beijing: A case study, *Sci Total Environ*, 800, 148868,
842 10.1016/j.scitotenv.2021.148868, 2021.

843 Tan, Z., Lu, K., Jiang, M., Su, R., Wang, H., Lou, S., Fu, Q., Zhai, C., Tan, Q., Yue, D., Chen, D., Wang, Z.,
844 Xie, S., Zeng, L., and Zhang, Y.: Daytime atmospheric oxidation capacity in four Chinese megacities
845 during the photochemically polluted season: a case study based on box model simulation, *Atmos Chem
846 Phys*, 19, 3493-3513, 10.5194/acp-19-3493-2019, 2019a.

847 Tan, Z., Fuchs, H., Lu, K., Hofzumahaus, A., Bohn, B., Broch, S., Dong, H., Gomm, S., Haeseler, R., He,
848 L., Holland, F., Li, X., Liu, Y., Lu, S., Rohrer, F., Shao, M., Wang, B., Wang, M., Wu, Y., Zeng, L., Zhang,
849 Y., Wahner, A., and Zhang, Y.: Radical chemistry at a rural site (Wangdu) in the North China Plain:
850 observation and model calculations of OH, HO₂ and RO₂ radicals, *Atmos Chem Phys*, 17, 663-690,
851 10.5194/acp-17-663-2017, 2017a.

852 Tan, Z. F., Lu, K. D., Dong, H. B., Hu, M., Li, X., Liu, Y. H., Lu, S. H., Shao, M., Su, R., Wang, H. C., Wu,
853 Y. S., Wahner, A., and Zhang, Y. H.: Explicit diagnosis of the local ozone production rate and the
854 ozone-NO_x-VOC sensitivities, *Sci. Bull.*, 63, 1067-1076, 10.1016/j.scib.2018.07.001, 2018.

855 Tan, Z. F., Lu, K. D., Hofzumahaus, A., Fuchs, H., Bohn, B., Holland, F., Liu, Y. H., Rohrer, F., Shao, M.,
856 Sun, K., Wu, Y. S., Zeng, L. M., Zhang, Y. S., Zou, Q., Kiendler-Scharr, A., Wahner, A., and Zhang, Y. H.:
857 Experimental budgets of OH, HO₂, and RO₂ radicals and implications for ozone formation in the Pearl
858 River Delta in China 2014, *Atmos Chem Phys*, 19, 7129-7150, 10.5194/acp-19-7129-2019, 2019b.

859 Tan, Z. F., Fuchs, H., Lu, K. D., Hofzumahaus, A., Bohn, B., Broch, S., Dong, H. B., Gomm, S., Haseler, R.,
860 He, L. Y., Holland, F., Li, X., Liu, Y., Lu, S. H., Rohrer, F., Shao, M., Wang, B. L., Wang, M., Wu, Y. S.,
861 Zeng, L. M., Zhang, Y. S., Wahner, A., and Zhang, Y. H.: Radical chemistry at a rural site (Wangdu) in the
862 North China Plain: observation and model calculations of OH, HO₂ and RO₂ radicals, *Atmos Chem Phys*,
863 17, 663-690, 10.5194/acp-17-663-2017, 2017b.

864 Wang, F., Hu, R., Xie, P., Wang, Y., Chen, H., Zhang, G., and Liu, W.: Calibration source for OH radical
865 based on synchronous photolysis, *Acta Phys Sin-Ch Ed*, 69, 2020.

866 Wang, F. Y., Hu, R. Z., Chen, H., Xie, P. H., Wang, Y. H., Li, Z. Y., Jin, H. W., Liu, J. G., and Liu, W. Q.:
867 Development of a field system for measurement of tropospheric OH radical using laser-induced
868 fluorescence technique, *Opt. Express*, 27, A419-A435, 10.1364/oe.27.00a419, 2019a.

869 Wang, H., Lu, K., Tan, Z., Chen, X., Liu, Y., and Zhang, Y.: Formation mechanism and control strategy for
870 particulate nitrate in China, *Journal of Environmental Sciences*, 10.1016/j.jes.2022.09.019, 2022a.

871 Wang, H., Ma, X., Tan, Z., Wang, H., Chen, X., Chen, S., Gao, Y., Liu, Y., Liu, Y., Yang, X., Yuan, B., Zeng,
872 L., Huang, C., Lu, K., and Zhang, Y.: Anthropogenic monoterpenes aggravating ozone pollution, *Natl. Sci.
873 Rev.*, 9, 2022b.

874 Wang, S.-n., Wu, R.-r., and Wang, L.-m.: Role of Hydrogen Migrations in Carbonyl Peroxy Radicals in the
875 Atmosphere, *Chinese J Chem Phys*, 32, 457-466, 10.1063/1674-0068/cjcp1811265, 2019b.

876 Wang, T., Xue, L., Feng, Z., Dai, J., Zhang, Y., and Tan, Y.: Ground-level ozone pollution in China: a
877 synthesis of recent findings on influencing factors and impacts, *Environmental Research Letters*,
878 10.1088/1748-9326/ac69fe, 2022c.

879 Wang, W., Yuan, B., Su, H., Cheng, Y., Qi, J., Wang, S., Song, W., Wang, X., Xue, C., Ma, C., Bao, F.,
880 Wang, H., Lou, S., and Shao, M.: A large role of missing volatile organic compound reactivity from
881 anthropogenic emissions in ozone pollution regulation, *Atmos Chem Phys*, 24, 4017-4027,
882 10.5194/acp-24-4017-2024, 2024.

883 Wang, W., Yuan, B., Peng, Y., Su, H., Cheng, Y., Yang, S., Wu, C., Qi, J., Bao, F., Huangfu, Y., Wang, C.,
884 Ye, C., Wang, Z., Wang, B., Wang, X., Song, W., Hu, W., Cheng, P., Zhu, M., Zheng, J., and Shao, M.:
885 Direct observations indicate photodegradable oxygenated volatile organic compounds (OVOCs) as larger
886 contributors to radicals and ozone production in the atmosphere, *Atmos Chem Phys*, 22, 4117-4128,
887 10.5194/acp-22-4117-2022, 2022d.

888 Wang, Y., Hu, R., Xie, P., Chen, H., Wang, F., Liu, X., Liu, J., and Liu, W.: Measurement of tropospheric
889 HO₂ radical using fluorescence assay by gas expansion with low interferences, *J Environ Sci (China)*, 99,
890 40-50, 10.1016/j.jes.2020.06.010, 2021.

891 Whalley, L. K., Blitz, M. A., Desservettaz, M., Seakins, P. W., and Heard, D. E.: Reporting the sensitivity
892 of laser-induced fluorescence instruments used for HO₂ detection to an interference from RO₂ radicals and
893 introducing a novel approach that enables HO₂ and certain RO₂ types to be selectively measured, *Atmos
894 Meas Tech*, 6, 3425-3440, 10.5194/amt-6-3425-2013, 2013.

895 Whalley, L. K., Stone, D., Dunmore, R., Hamilton, J., Hopkins, J. R., Lee, J. D., Lewis, A. C., Williams, P.,
896 Kleffmann, J., Laufs, S., Woodward-Massey, R., and Heard, D. E.: Understanding in situ ozone production
897 in the summertime through radical observations and modelling studies during the Clean air for London
898 project (ClearfLo), *Atmos Chem Phys*, 18, 2547-2571, 10.5194/acp-18-2547-2018, 2018.

899 Whalley, L. K., Slater, E. J., Woodward-Massey, R., Ye, C., Lee, J. D., Squires, F., Hopkins, J. R., Dunmore,
900 R. E., Shaw, M., Hamilton, J. F., Lewis, A. C., Mehra, A., Worrall, S. D., Bacak, A., Bannan, T. J., Coe, H.,
901 Percival, C. J., Ouyang, B., Jones, R. L., Crilley, L. R., Kramer, L. J., Bloss, W. J., Vu, T., Kotthaus, S.,
902 Grimmond, S., Sun, Y., Xu, W., Yue, S., Ren, L., Acton, W. J. F., Hewitt, C. N., Wang, X., Fu, P., and Heard,
903 D. E.: Evaluating the sensitivity of radical chemistry and ozone formation to ambient VOCs and NO_x in
904 Beijing, *Atmos Chem Phys*, 21, 2125-2147, 10.5194/acp-21-2125-2021, 2021.

905 Woodward-Massey, R., Sommariva, R., Whalley, L. K., Cryer, D. R., Ingham, T., Bloss, W. J., Ball, S. M.,
906 Cox, S., Lee, J. D., Reed, C. P., Crilley, L. R., Kramer, L. J., Bandy, B. J., Forster, G. L., Reeves, C. E.,
907 Monks, P. S., and Heard, D. E.: Radical chemistry and ozone production at a UK coastal receptor site,
908 *Atmos Chem Phys*, 23, 14393-14424, 10.5194/acp-23-14393-2023, 2023.

909 Yang, X., Li, Y., Ma, X., Tan, Z., Lu, K., and Zhang, Y.: Unclassical Radical Generation Mechanisms in the
910 Troposphere: A Review, *Environ Sci Technol*, 10.1021/acs.est.4c00742, 2024a.

911 Yang, X., Lu, K., Ma, X., Gao, Y., Tan, Z., Wang, H., Chen, X., Li, X., Huang, X., He, L., Tang, M., Zhu,
912 B., Chen, S., Dong, H., Zeng, L., and Zhang, Y.: Radical chemistry in the Pearl River Delta: observations
913 and modeling of OH and HO₂ radicals in Shenzhen in 2018, *Atmos Chem Phys*, 22, 12525-12542,
914 10.5194/acp-22-12525-2022, 2022.

915 Yang, X., Wang, H., Lu, K., Ma, X., Tan, Z., Long, B., Chen, X., Li, C., Zhai, T., Li, Y., Qu, K., Xia, Y.,
916 Zhang, Y., Li, X., Chen, S., Dong, H., Zeng, L., and Zhang, Y.: Reactive aldehyde chemistry explains the
917 missing source of hydroxyl radicals, *Nat Commun*, 15, 1648, 10.1038/s41467-024-45885-w, 2024b.

918 Yang, X., Lu, K., Ma, X., Liu, Y., Wang, H., Hu, R., Li, X., Lou, S., Chen, S., Dong, H., Wang, F., Wang, Y.,
919 Zhang, G., Li, S., Yang, S., Yang, Y., Kuang, C., Tan, Z., Chen, X., Qiu, P., Zeng, L., Xie, P., and Zhang, Y.:
920 Observations and modeling of OH and HO₂ radicals in Chengdu, China in summer 2019, *The Science of
921 the total environment*, 772, 144829-144829, 10.1016/j.scitotenv.2020.144829, 2021a.

922 Yang, Y., Li, X., Zu, K., Lian, C., Chen, S., Dong, H., Feng, M., Liu, H., Liu, J., Lu, K., Lu, S., Ma, X.,
923 Song, D., Wang, W., Yang, S., Yang, X., Yu, X., Zhu, Y., Zeng, L., Tan, Q., and Zhang, Y.: Elucidating the
924 effect of HONO on O₃ pollution by a case study in southwest China, *Sci Total Environ*, 756, 144127,
925 10.1016/j.scitotenv.2020.144127, 2021b.

926 Yugo Kanaya, Renqiu Cao, Hajime Akimoto, Masato Fukuda, Yuichi Komazaki, Yoko Yokouchi, Makoto
927 Koike, Hiroshi Tanimoto, Nobuyuki Takegawa, and Kondo, a. Y.: Urban photochemistry in central Tokyo:
928 1. Observed and modeled OH and HO₂ radical concentrations during the winter and summer of 2004, *J
929 Geophys Res-Atmos*, 112, 20, 10.1029/2007JD008670, 2007.

930 Yugo Kanaya, R. C., Shungo Kato, Yuko Miyakawa, Yoshizumi Kajii, Hiroshi and Tanimoto, Y. Y.,
931 Michihiro Mochida, Kimitaka Kawamura, Hajime Akimoto: Chemistry of OH and HO₂ radicals observed

932 at Rishiri Island, Japan, in September 2003: Missing daytime sink of HO₂ and positive nighttime
933 correlations with monoterpene, *J Geophys Res-Atmos*, 112, 10.1029/2006id007987, 2007.
934 Zhang, G., Hu, R., Xie, P., Lou, S., Wang, F., Wang, Y., Qin, M., Li, X., Liu, X., Wang, Y., and Liu, W.:
935 Observation and simulation of HO_x radicals in an urban area in Shanghai, China, *Sci Total Environ*, 810,
936 152275, 10.1016/j.scitotenv.2021.152275, 2022a.
937 Zhang, G., Hu, R., Xie, P., Lu, K., Lou, S., Liu, X., Li, X., Wang, F., Wang, Y., Yang, X., Cai, H., Wang, Y.,
938 and Liu, W.: Intercomparison of OH radical measurement in a complex atmosphere in Chengdu, China, *Sci
939 Total Environ*, 155924, 10.1016/j.scitotenv.2022.155924, 2022b.
940